Three-dimensional constitutive model for shape memory polymers using multiplicative decomposition of the deformation gradient and shape memory strains

Haedong Park , Philip Harrison , Zaoyang Guo ,
Myoung-Gue Lee , Woong-Ryeol Yu

PII: S0167-6636(15)00223-9
DOI: 10.1016/j.mechmat.2015.10.014
Reference: MECMAT 2499

To appear in: *Mechanics of Materials*

Received date: 10 June 2015
Revised date: 21 October 2015
Accepted date: 22 October 2015

Please cite this article as: Haedong Park , Philip Harrison , Zaoyang Guo , Myoung-Gue Lee , Woong-Ryeol Yu , Three-dimensional constitutive model for shape memory polymers using multiplicative decomposition of the deformation gradient and shape memory strains, *Mechanics of Materials* (2015), doi: 10.1016/j.mechmat.2015.10.014

Highlights

- A 3D constitutive equation for SMPs based on a two-phase is developed.
- Shape memory strain is introduced to simulate the shape memory effect.
- The total deformation gradient is multiplicatively decomposed into each element.
- Shape memory strain is determined by assuming proportionality to the total deformation.
- The simulation results are in good agreement with experiments.

Three-dimensional constitutive model for shape memory polymers using multiplicative decomposition of the deformation gradient and shape memory strains

Haedong Park[1,+], Philip Harrison[2], Zaoyang Guo[3], Myoung-Gue Lee[4], Woong-Ryeol Yu[1]*

[1] Department of Materials Science and Engineering and Research Institute of Advanced Materials, Seoul National University, 1 Gwanak-ro, Gwanak-gu, Seoul 151-742, Republic of Korea
[2] School of Engineering, University of Glasgow, Glasgow G12 8QQ, UK
[3] Department of Engineering Mechanics, Chongqing University, Chongqing, 400044, China
[4] Department of Materials Science and Engineering, Korea University, Anam-dong, Seongbuk-gu, Seoul 136-701, Republic of Korea
* Corresponding author (woongryu@snu.ac.kr)
+ Present address: Computational Science Center, Korea Institute of Science and Technology, Hwarang-ro 14-gil 5, Seongbuk-gu, Seoul 136-791, Republic of Korea

Abstract

Using a two-phase (rubbery and glassy) phenomenological model and shape memory strains, a three-dimensional constitutive model for shape memory polymers (SMPs) was developed that can simulate multi-axial and large deformation behavior (up to 200% of strain) of SMPs. To derive a constitutive equation, the total deformation gradient was multiplicatively decomposed into hyperelastic, viscoelastic, viscoplastic, and shape memory strains using Helmholtz free energy and the Clausius-Duhem inequality. The shape memory strain was determined from the total deformation by assuming proportionality to the total deformation. The developed constitutive model was validated by simulating the shape memory behavior of SMPs using a finite element method and comparing the simulation results with experiments. Finally, the capabilities of the constitutive equation were demonstrated by simulating constrained shape recovery behavior of SMPs.

Keywords: shape memory polymers, constitutive model, large deformation, multiplicative decomposition, shape memory strain

1. Introduction

Shape memory polymers (SMPs) are smart materials that can recover a permanent or memorized shape from a temporarily fixed one in response to external stimulus, such as heat (Leng et al., 2011). Many experimental studies have been carried out to characterize the macro- and microscopic material properties of SMPs and to investigate one-way shape memory in SMPs. Various SMPs have been studied, including epoxy resin (Chen et al., 2014; Song et al., 2011), polyurethanes (Hong et al., 2007; Tobushi et al., 1996; Wang et al., 2010), polyimide (Xiao et al., 2015), commercially available SMPs (Richard and Lisa Mauck, 2008), and poly(cyclooctene) (PCO) (Liu et al., 2002). Two-way shape memory, i.e., reversible deformation behavior in response to an on-off stimulus, has also been demonstrated using one-way SMPs and bias loads (Chung et al., 2007; Hong et al., 2010; Pandini et al., 2012). Due to these fascinating properties, SMPs are promising for use in many applications, including aerospace devices (Liu et al., 2014), self-healing medical materials (Li and Shojaei, 2012; Xu and Li, 2010), smart biomedical stents (El Feninat et al., 2002; Kim et al., 2010a; Reese et al., 2010), fiber-reinforced SMP composites (Lan et al., 2014; Tan et al., 2014; Zhang et al., 2015), particle-reinforced SMP composites (Hong et al., 2008), metal-SMP composites (Wang and Li, 2011), Alloy-SMP composite (Qiao et al., 2013), and 4D printings (Ge et al., 2014; Ge et al., 2013; Yu et al., 2015).

Despite the efforts of many experimental studies, the complex thermo-mechanical behavior of SMPs has limited their constitutive modeling. Simple rheological models, which are valid only for limited materials under one-dimensional (1D) stress, were proposed as early as 2000 (Abrahamson et al., 2003; Bhattacharyya and Tobushi, 2000; Lin and Chen, 1999; Morshedian et al., 2005; Tobushi et al., 2001). These rheological models adopt spring, dashpot, and frictional elements to simulate thermo-mechanical deformation behavior of SMPs.

Multi-phase SMP models, such as those assuming that the internal structure of SMPs consists of hard and soft segments, have also been presented (Lee et al., 2004; Ping et al., 2007). These multi-phase models successfully simulate the deformation behavior of 1D SMPs (Gilormini and Diani, 2012; Guo et al., 2015; Kazakevičiūtė-Makovska et al., 2014; Kim et al., 2010b), including the mechanical behavior of braided SMP stents (Kim et al., 2010a). However, the SMP models were described in 1D, making it difficult to develop 3D constitutive equations.

Most previously developed multi-phase constitutive models are phenomenological models that capture the thermo-mechanical deformation behavior of SMPs using a continuum element (Chen and Lagoudas, 2008a, b; Diani et al., 2006; Guo et al., 2014; Heuchel et al., 2013; Liu et al., 2006; Qi et al., 2008; Wang et al., 2009). The common feature of these phenomenological multi-phase models is generalization of three-dimensional (3D) problems based on continuum mechanics. Another common feature is utilization of the mixture rule to describe the volume fractions of the constituent phases (e.g., rubbery and glassy phases) as a function of temperature, thereby enabling the calculation of free energy, strain, and stress. Those models utilize the concept of strain storage (or non-mechanical strain), which has been often introduced to account for the shape memory effect (Baghani et al., 2014a; Chen and Lagoudas, 2008a, b; Diani et al., 2006; Guo et al., 2014; Liu et al., 2006). Previously developed multi-phase phenomenological constitutive models can be implemented into finite element analysis (FEA) software. However, most existing 3D models have assumed small deformation and were validated using either 1D uniaxial tests or limited 3D problems which deal with only simple mechanical behavior like uniaxial extension or compression with 3D constitutive equations.

In addition to the strain storage concept, other approaches have been used for explaining the shape memory effect in SMPs. For example, the temporarily fixed shape of SMPs has

been modeled using their crystallization behavior (Barot and Rao, 2006) and, in particular, strain- or stress-induced crystallization processes (Barot et al., 2008; Li and Shojaei, 2012; Rao and Rajagopal, 2001; Richard and Lisa Mauck, 2008; Westbrook et al., 2010). Shape memory has also been modeled on the temperature-induced changes in SMP microscopic structures (Ghosh and Srinivasa, 2013, 2014; Gu et al., 2015; Nguyen et al., 2008; Nguyen et al., 2010; Srivastava et al., 2010; Westbrook et al., 2011; Xiao et al., 2013). These temperature-dependent models were based on the well-known Arruda-Boyce model (Arruda and Boyce, 1993), which includes detailed microscopic features of SMPs. Recently, complex problems involving beam, film, and stents have been efficiently analyzed using such numerical methods (Baghani, 2014; Baghani et al., 2014b; Baghani et al., 2012a; Baghani et al., 2012b; Baghani et al., 2012c; Diani et al., 2012; Xiao and Nguyen, 2013). However, those studies did not propose an appropriate model for large deformation.

In this work, a new constitutive model was developed, focusing on (1) three-dimensional theory, (2) large deformation, (3) multi-dimensional problem. The new 3D constitutive model of SMPs was developed based on a two-phase assumption of the SMP microstructure (rubbery and glassy phases). Both rubbery and glassy phases were modeled using a visco-hyperelastic equation. To describe the large deformation behavior of SMPs, the deformation gradient was multiplicatively decomposed into the deformation gradient of each phase. The shape memory effect was then modeled using 3D shape memory strains occurring in the glassy phase, the formulation of which was carried out using the principal axes and stretches of the total deformation. The material parameters for newly developed constitutive equations were determined using the uniaxial and thermo-mechanical cyclic experiments. Finally, 3D finite element simulations were carried out to validate the developed constitutive models.

2. 3D constitutive model for shape memory polymers

2.1 Basic considerations for constitutive modeling of SMPs

Thermo-responsive SMPs possess the transition temperature (T_{tr}) beyond which they exhibit the rubbery behavior due to the entropic elasticity of polymer molecules. Upon cooling, the rubbery behavior of such SMPs turn into the glassy one, losing the entropic elasticity. Using this microstructural change of SMPs, we can memorize the deformation into the SMPs. For example, we can apply some deformations to SMPs at a temperature (usually, $T_h = T_{tr}$ +15 ºC) higher than T_{tr}. Keeping the deformation, the SMPs are then cooled down to a temperature (usually, $T_l = T_{tr}$ -15 ºC). Subsequent unloading cannot return the shape of the SMPs to original shape before the loading because the SMP molecules are frozen due to the lowered temperature and loose the entropic elasticity, i.e., the deformed shape of SMPs remains. Upon heating (usually to T_h), the SMPs gain the entropic elasticity, returning to the original shape.

To develop a constitutive model for describing the thermo-mechanical behavior of such thermo-responsive SMPs mathematically, two-phase models consisting of rubbery and glassy phases have been used, e.g., a parallel connection of rubbery and glassy phases (Kim et al., 2010b) (see Fig. 1). At T_h, the rubbery phase is the dominant microstructure, while the glassy phase is dominant at T_l. The switching between these two phases is modeled by the volume fractions of each phase, e.g., at T_h, the volume fractions of the rubbery and glassy phases are 1 and 0, respectively. We followed this methodology to derive the constitutive equation of SMPs.

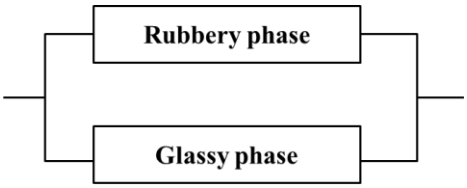

Fig. 1. Parallel connection model of rubbery and glassy phases to describe the shape memory behavior of SMPs phenomenologically.

Next, a rheological model is considered for the rubbery phase of SMPs. Fig. 2(a) shows the stress and strain curve of a SMP (poly(cyclooctene), see Section 3.1 for detailed information) when uniaxial tension, stress relaxation, and unloading were consecutively applied to the SMP, at T_h. The non-linear elastic behavior was observed, implying that the rheological model of the rubbery phase should have hyperelastic springs. The stress relaxation occurred when the strain was kept, and upon unloading the strain went to almost zero, suggesting a parallel connection of the spring and the dashpot. Herein, Poynting-Thomson model was used for the rheological model for the rubbery phase of SMPs, as shown in Fig. 2(b).

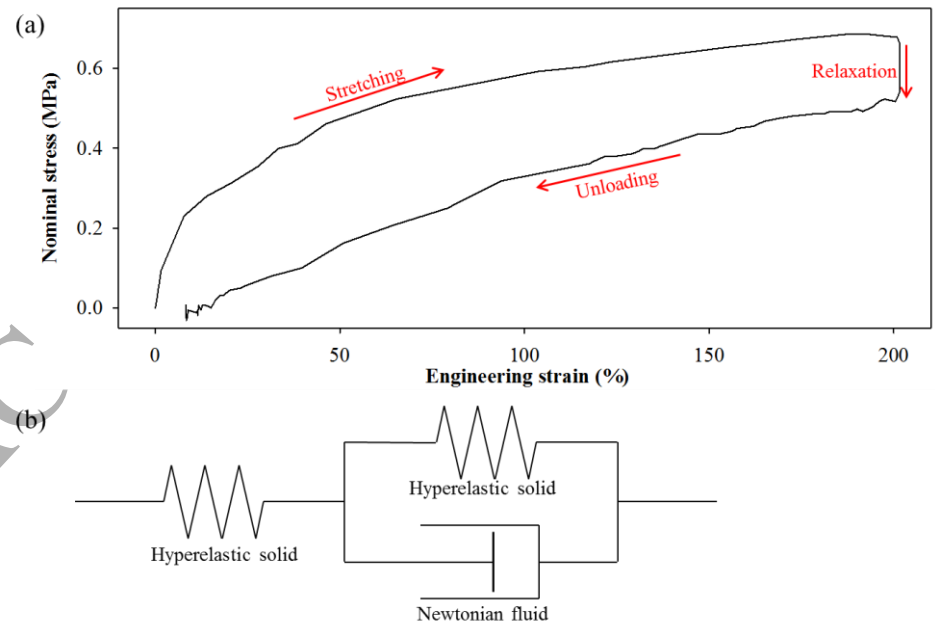

Fig. 2. (a) Uniaxial loading-relaxation-unloading behavior of a SMP at its T_h. (b) Poynting-Thomson model for the rubbery phase of SMPs.

Next, a rheological model is considered for the glassy phase of SMPs. At T_l, the non-linear elasticity and relaxation were observed (Fig. 3(a)), similarly to the rubbery phase. Contrary to the recovered strain of the rubbery phase upon unloading, the permanent deformation was observed, implying the inclusion of (visco)plastic element in the rheological model of the glassy phase. Therefore, the glassy phase was modeled using both Poynting-Thomson model and viscoplastic element, as shown in Fig. 3(b). Another element (so called, shape memory strain element) was added in the rheological model of the glassy phase because the shape memory effect was involved in the cooling, the relaxation, the unloading, and the heating processes (see Fig. 4), where the rubbery phase is not completely dominant.

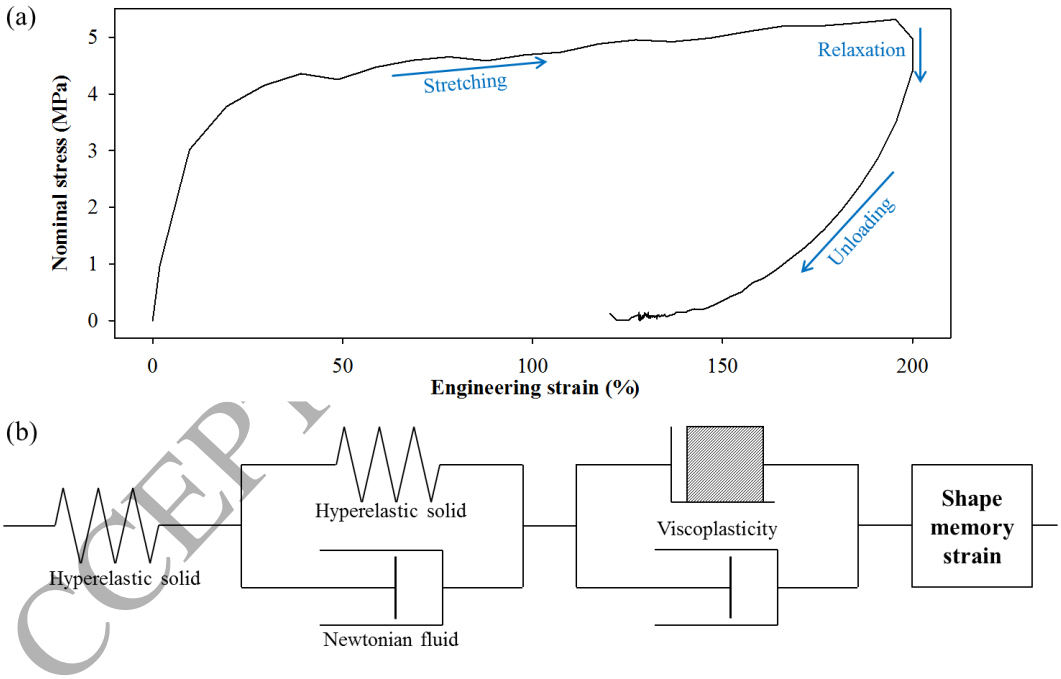

Fig. 3. (a) Uniaxial loading-relaxation-unloading behavior of a SMP at its T_l. (b) Rheological model for the glassy phase of SMPs.

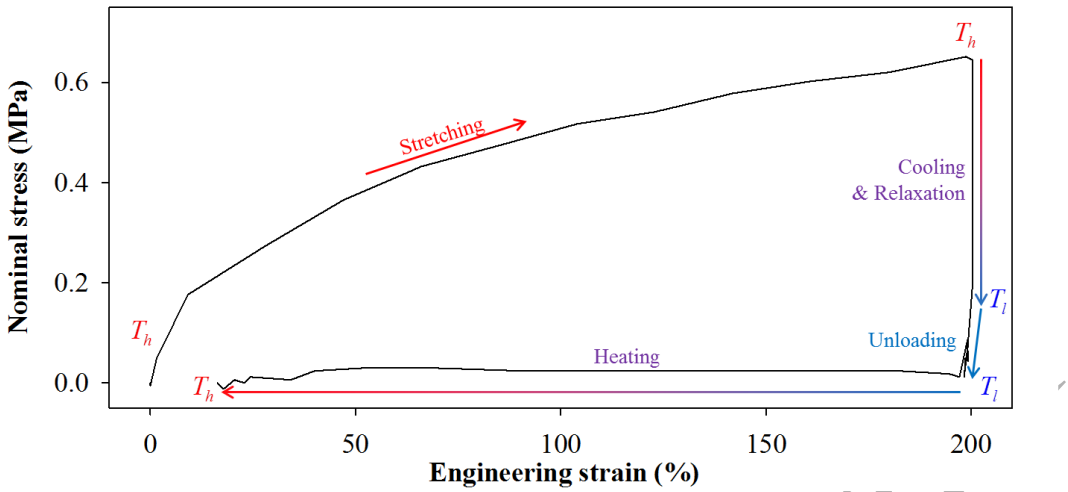

Fig. 4. Thermo-mechanical cyclic behavior of a SMP. At T_h the SMP was extended up to 200%. Keeping the strain, the SMP was cooled down to T_l and unloaded. Finally, the SMP was heated again to T_h, recovering the strain.

Finally, a phenomenological and rheological model consisting of two parallel phases (rubbery and glassy phases) for describing the thermo-mechanical deformation behavior of SMPs at the continuum level is suggested as in Fig. 5. In this study, an isostrain model, i.e., parallel combination of the two phases, is used, but an isostress approach can be also used. For small strain behavior of shape memory polymer, we developed 1D phenomenological models using both isostrain and isotress approaches, demonstrating that both models can simulate the shape memory behavior appropriately (Kim et al., 2010b). In this study, the deformation gradient will be multiplicatively decomposed into the deformation gradient of each phase to describe the large deformation behavior of shape memory polymers. For an isostrain approach, the total deformation gradient can be decomposed as Equation (1) in Section 2.2, however, for an isostress approach, the total deformation gradient may be decomposed into a product of all deformation gradients. The isostrain approach is more convenient to determine the decomposed deformation gradient than an isostress approach. Therefore, we will focus on the isostrain model in Fig. 5.

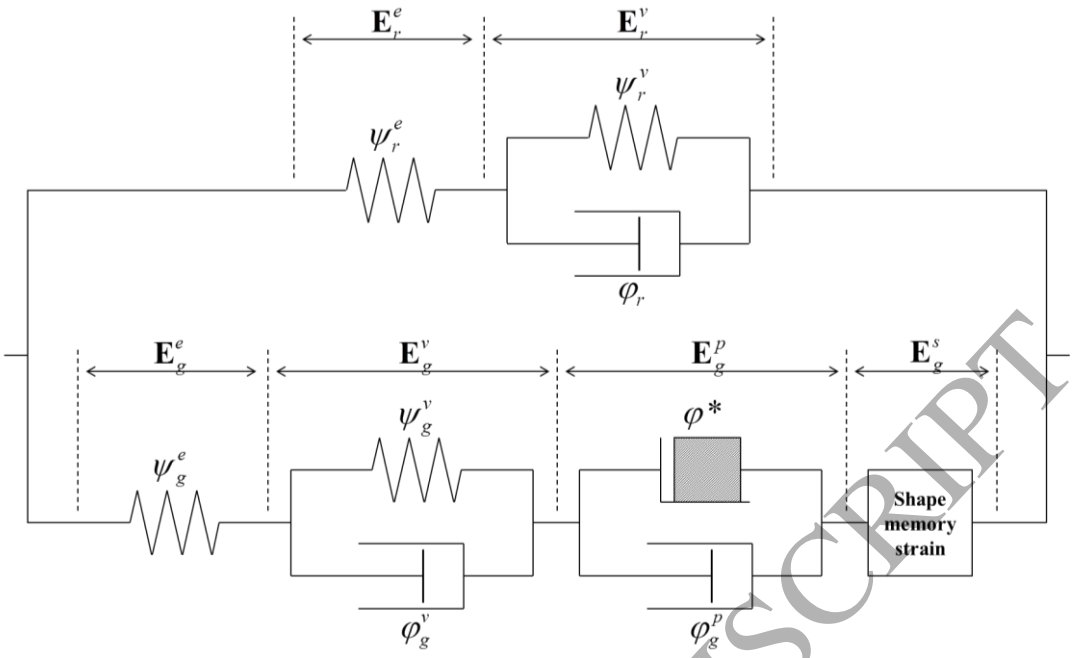

Fig. 5. A phenomenological and rheological two-phase model for SMPs which consists of rubbery (top) and glassy (bottom) phases.

2.2 Derivation of constitutive equation of SMPs

The stress and strain relationship are derived with respect to the large deformation of SMPs based on the model built in Fig. 5. The total deformation gradient is multiplicatively decomposed into the elastic and other deformation gradients as follows (Lee, 1969):

$$\begin{aligned}\mathbf{F} &= \mathbf{F}_r^e \mathbf{F}_r^v \\ &= \mathbf{F}_g^e \mathbf{F}_g^v \mathbf{F}_g^p \mathbf{F}_g^s\end{aligned} \tag{1}$$

where the superscripts *e*, *v*, *p* and *s* represent the hyperelastic spring, the viscoelastic component (parallel connection of the hyperelastic spring and a dashpot), the viscoplastic component, and the shape memory strain element, respectively. The subscripts *r* and *g* indicate the rubbery and glassy phases, respectively. The original decomposition ($\mathbf{F} = \mathbf{F}^e \mathbf{F}^p$) of the deformation gradient proposed by Lee (Lee, 1969) or similar decompositions by some studies (Baghani et al., 2012a; Laiarinandrasana et al., 2003; Lejeunes et al., 2011; Qi et al., 2008; Westbrook et al., 2011) were modified to include the contributions of hyperelastic, viscoelas-

tic, viscoplastic elements and shape memory strains. Prior to the decomposition of Equation (1), the second Piola-Kirchhoff stresses and the mechanical dissipation of the rubbery and glassy phases are defined as follows.

If the volume fractions of the rubbery and glassy phases of an SMP are denoted by ξ_r and ξ_g, respectively, and if summation of these volume fractions is unity, i.e., $\xi_r + \xi_g = 1$, the second Piola-Kirchhoff stress can be decomposed into the stress associated with the rubbery and glassy stresses:

$$\mathbf{S} = \xi_r(T)\mathbf{S}_r + \xi_g(T)\mathbf{S}_g \tag{2}$$

where $\mathbf{S}_r$ and $\mathbf{S}_g$ are the second Piola-Kirchhoff stresses of the rubbery and glassy phases, respectively. In this study, assuming that the volume fraction of the glassy phase in Equation (2) is determined by only temperature, the following relationship was used. A detailed procedure to determine the parameters (*b*, *c*, T_{tr}, and *d)* is provided in Appendix A.

$$\xi_g = \begin{cases} 1 & 1 < \xi_g^0 \\ \xi_g^0 & 0 \le \xi_g^0 \le 1 \\ 0 & \xi_g^0 < 0 \end{cases} \quad \text{with} \quad \xi_g^0 = \frac{b}{1+\exp\left(c\left(T - T_{tr}\right)\right)} - d \tag{3}$$

All dashpots in this model are set as Newtonian fluid. Then, the mechanical dissipation of the rubbery phase can be expressed as a pseudo-potential of dissipation (Boukamel et al., 1997; Meo et al., 2002):

$$\varphi_r = \frac{1}{2}\mu_r \dot{\mathbf{C}}_r^v : \dot{\mathbf{C}}_r^v \tag{4}$$

where μ_r is the viscosity of the rheological model for the rubbery phase and $\mathbf{C}_r^v \left(= \left(\mathbf{F}_r^v\right)^T \left(\mathbf{F}_r^v\right)\right)$ is the right Cauchy-Green tensor of viscoelastic element of the model (see

Fig. 5). Similarly, the mechanical dissipation of the glassy phase can be written, however, the viscoplastic component and the shape memory strain element may induce additional mechanical dissipation as follows:

$$\varphi_g = \frac{1}{2}\mu_g \dot{\mathbf{C}}_g^v : \dot{\mathbf{C}}_g^v + \varphi_g^p\left(\dot{\mathbf{F}}_g^p\right) + \varphi_g^s\left(\mathbf{F}_g^s\right) \tag{5}$$

where μ_g and $\mathbf{C}_g^v$ are the viscosity and the right Cauchy-Green tensor of the second element in the rheological model for the glassy phase. φ_g^p and φ_g^s are the mechanical dissipations of the viscoplastic element and the shape memory strain element, respectively.

Meanwhile all hyperelastic springs in this study were assumed as a Mooney-Rivlin solid in first order:

$$\psi_j^k\left(\bar{I}_j^k, \overline{II}_j^k, J_j^k\right) = C_{10,j}^k\left(\bar{I}_j^k - 3\right) + C_{01,j}^k\left(\overline{II}_j^k - 3\right) + \frac{\kappa_j^k}{2}\left(J_j^k - 1\right)^2 \tag{6}$$

where $\bar{I}_j^k$, $\overline{II}_j^k$, and J_j^k are incompressible invariants and $C_{10,j}^k$, $C_{01,j}^k$, and κ_j^k are material coefficients of element *k* in phase *j*. Note that the superscript *k* can be either *e* or *v* while *j* can be either *r* or *g*.

The multiplicative decomposition of the deformation gradient in Equation (1) was carried out by defining Helmholtz free energy and using the Clausis-Duhem inequality as follows. Helmholtz free energy (per unit volume), ψ, can be additively expressed as follows:

$$\begin{aligned}\psi &= \xi_r \psi_r + \xi_g \psi_g \\ &= \xi_r(T)\psi_r\left(\mathbf{C}, \mathbf{C}_r^v\right) + \xi_g(T)\psi_g\left(\mathbf{C}, \mathbf{C}_g^v, \mathbf{C}_g^p, \mathbf{C}_g^s\right)\end{aligned} \tag{7}$$

where $\mathbf{C} = \mathbf{F}^T\mathbf{F}$ is the right Cauchy-Green tensor. Then, the Clausius-Duhem inequality can be expressed in terms of the second Piola-Kirhoff stress ($\mathbf{S}$) and Helmholtz free energy as follows (Haupt, 2002; Helm and Haupt, 2003; Meo et al., 2002):

$$-\dot{\psi}-\rho\dot{T}\eta-\frac{\mathbf{q}\cdot\nabla T}{T}+\frac{1}{2}\mathbf{S}:\dot{\mathbf{C}}\geq 0 \tag{8}$$

where T is the temperature, ρ the mass density, $\mathbf{q}$ the heat flux, and η represents the entropy. Equations (2), (7), and $\mathbf{q}=-q\nabla T$ are substituted into Equation (8), deriving the following inequality (Laiarinandrasana et al., 2003; Lejeunes et al., 2011):

$$\begin{aligned}&\xi_r\left\{\left(\frac{1}{2}\mathbf{S}_r-\frac{\partial\psi_r}{\partial\mathbf{C}}\right):\dot{\mathbf{C}}-\frac{\partial\psi_r}{\partial\mathbf{C}_r^v}:\dot{\mathbf{C}}_r^v\right\}\\&+\xi_g\left\{\left(\frac{1}{2}\mathbf{S}_g-\frac{\partial\psi_g}{\partial\mathbf{C}}\right):\dot{\mathbf{C}}-\frac{\partial\psi_g}{\partial\mathbf{C}_g^v}:\dot{\mathbf{C}}_g^v-\frac{\partial\psi_g}{\partial\mathbf{C}_g^p}:\dot{\mathbf{C}}_g^p-\frac{\partial\psi_g}{\partial\mathbf{C}_g^s}:\dot{\mathbf{C}}_g^s\right\}\\&-\left\{\frac{\partial\psi}{\partial T}+\rho\eta\right\}\dot{T}+\frac{q\left|\nabla T\right|^2}{T}\geq 0\end{aligned} \tag{9}$$

or

$$\xi_r\varphi_r+\xi_g\varphi_g+\varphi_{th}\geq 0 \tag{10}$$

where φ_{th} is the thermal dissipation. The three dissipation quantities, each of which is equal to or larger than zero, are expressed by the following equations:

$$\varphi_r=\left(\frac{1}{2}\mathbf{S}_r-\frac{\partial\psi_r}{\partial\mathbf{C}}\right):\dot{\mathbf{C}}-\frac{\partial\psi_r}{\partial\mathbf{C}_r^v}:\dot{\mathbf{C}}_r^v \tag{11}$$

$$\varphi_g=\left(\frac{1}{2}\mathbf{S}_g-\frac{\partial\psi_g}{\partial\mathbf{C}}\right):\dot{\mathbf{C}}-\frac{\partial\psi_g}{\partial\mathbf{C}_g^v}:\dot{\mathbf{C}}_g^v-\frac{\partial\psi_g}{\partial\mathbf{C}_g^p}:\dot{\mathbf{C}}_g^p-\frac{\partial\psi_g}{\partial\mathbf{C}_g^s}:\dot{\mathbf{C}}_g^s \tag{12}$$

$$\varphi_{th}=-\left\{\frac{\partial\psi}{\partial T}+\rho\eta\right\}\dot{T}+q\frac{\left|\nabla T\right|^2}{T} \tag{13}$$

To satisfy above inequality for arbitrary $\dot{\mathbf{C}}$, $\dot{\mathbf{C}}_r^v$, $\dot{\mathbf{C}}_g^v$, $\dot{\mathbf{C}}_g^p$, $\dot{\mathbf{C}}_g^s$, and $\dot{T}$, the following relations should be also satisfied:

$$\frac{1}{2}\mathbf{S}_r-\frac{\partial\psi_r}{\partial\mathbf{C}}=\frac{\partial\varphi_r}{\partial\dot{\mathbf{C}}}=0 \tag{14}$$

$$-\frac{\partial \psi_r}{\partial \mathbf{C}_r^v}=\frac{\partial \varphi_r}{\partial \dot{\mathbf{C}}_r^v}=\mu_r \dot{\mathbf{C}}_r^v \tag{15}$$

$$\frac{1}{2}\mathbf{S}_g-\frac{\partial \psi_g}{\partial \mathbf{C}}=\frac{\partial \varphi_g}{\partial \dot{\mathbf{C}}}=0 \tag{16}$$

$$-\frac{\partial \psi_g}{\partial \mathbf{C}_g^v}=\frac{\partial \varphi_g}{\partial \dot{\mathbf{C}}_g^v}=\mu_g \dot{\mathbf{C}}_g^v \tag{17}$$

$$-\frac{\partial \psi_g}{\partial \mathbf{C}_g^p}=\frac{\partial \varphi_g}{\partial \dot{\mathbf{C}}_g^p} \tag{18}$$

$$-\frac{\partial \psi_g}{\partial \mathbf{C}_g^s}=\frac{\partial \varphi_g}{\partial \dot{\mathbf{C}}_g^s} \tag{19}$$

The entropy relationship is given by

$$\eta=-\frac{1}{\rho}\frac{\partial \psi}{\partial T} \tag{20}$$

2.2.1 Decomposition of the deformation gradient of the rubbery phase

As shown in Fig. 5, the rubbery phase is modeled using a combination of a hyperelastic spring and a viscoelastic element (the parallel connection of a hyperelastic spring and a dash-pot of Newtonian fluid). The Helmholtz free energy of the rubbery phase is determined by these two elements in terms of the invariants of the right stretch tensors as follows:

$$\begin{aligned}\psi_r &= \psi_r^e\left(\mathbf{C},\mathbf{C}_r^v\right)+\psi_r^v\left(\mathbf{C}_r^v\right)\\ &= \psi_r^e\left(I_r^e, II_r^e, III_r^e\right)+\psi_r^v\left(I_r^v, II_r^v, III_r^v\right)\end{aligned} \tag{21}$$

Then, Equation (15) can be rewritten as

$$
\begin{aligned}
\mu_r \dot{\mathbf{C}}_r^v &= -\frac{\partial \psi_r}{\partial \mathbf{C}_r^v} \\
&= \left(\mathbf{C}_r^v\right)^{-1} \mathbf{C} \left\{ \left(\frac{\partial \psi_r^e}{\partial I_r^e} + I_r^e \frac{\partial \psi_r^e}{\partial II_r^e} \right) \mathbf{I} - \frac{\partial \psi_r^e}{\partial II_r^e} \left(\mathbf{C}_r^v\right)^{-1} \mathbf{C} \right\} \left(\mathbf{C}_r^v\right)^{-1} \\
&\quad + \frac{\partial \psi_r^e}{\partial III_r^e} III_r^e \left(\mathbf{C}_r^v\right)^{-1} \\
&\quad - \left\{ \left(\frac{\partial \psi_r^v}{\partial I_r^v} + I_r^v \frac{\partial \psi_r^v}{\partial II_r^v} \right) \mathbf{I} - \frac{\partial \psi_r^v}{\partial II_r^v} \mathbf{C}_r^v \right\} - \frac{\partial \psi_r^v}{\partial III_r^v} III_r^v \left(\mathbf{C}_r^v\right)^{-1}
\end{aligned}
\tag{22}
$$

Incompressible invariants ($\bar{I}_r^k$, $\bar{II}_r^k$, and J_r^k) (Bower, 2009) are then introduced where the superscript *k* is *e* or *v*, resulting in the final differential equation. Note that Equation (6) is used for all hyperelastic springs.

$$
\begin{aligned}
\mu_r \dot{\mathbf{C}}_r^v &= \left(J_r^e\right)^{-2/3} \left(\mathbf{C}_r^v\right)^{-1} \mathbf{C} \left\{ \left(C_{10,r}^e + \bar{I}_r^e C_{01,r}^e\right) \mathbf{I} - \left(J_r^e\right)^{-2/3} C_{01,r}^e \left(\mathbf{C}_r^v\right)^{-1} \mathbf{C} \right\} \left(\mathbf{C}_r^v\right)^{-1} \\
&\quad + \left\{ -\frac{1}{3} \left(\bar{I}_r^e C_{10,r}^e + 2\bar{II}_r^e C_{01,r}^e \right) + \frac{1}{2} \kappa_r^e J_r^e \left(J_r^e - 1 \right) \right\} \left(\mathbf{C}_r^v\right)^{-1} \\
&\quad - \left\{ \left(J_r^v\right)^{-2/3} \left(C_{10,r}^v + \bar{I}_r^v C_{01,r}^v\right) \mathbf{I} - \left(J_r^v\right)^{-4/3} C_{01,r}^v \mathbf{C}_r^v \right\} \\
&\quad - \left\{ -\frac{1}{3} \left(\bar{I}_r^v C_{10,r}^v + 2\bar{II}_r^v C_{01,r}^v \right) + \frac{1}{2} \kappa_r^v J_r^v \left(J_r^v - 1 \right) \right\} \left(\mathbf{C}_r^v\right)^{-1}
\end{aligned}
\tag{23}
$$

As Equation (23) is an ordinary differential equation of $\mathbf{C}_r^v$, it can be solved with the given total deformation ($\mathbf{C}\left(=\mathbf{F}^T\mathbf{F}\right)$), producing $\mathbf{C}_r^v$ and $\mathbf{F}_r^e$.

2.2.2 Decomposition of the deformation gradient of the glassy phase

The glassy phase consists of a hyperelastic spring, a viscoelastic element, a viscoplastic element, and a shape memory strain element, as shown in Fig. 5. The Helmholtz free energy of the glassy phase is written by the first two elements in terms of the invariants of the right stretch tensors as follows:

$$\begin{aligned}\psi_g &= \psi_g^e\left(\mathbf{C},\mathbf{C}_g^v,\mathbf{C}_g^p,\mathbf{C}_g^s\right)+\psi_g^v\left(\mathbf{C}_g^v\right)\\ &= \psi_g^e\left(I_g^e,II_g^e,III_g^e\right)+\psi_g^v\left(I_g^v,II_g^v,III_g^v\right)\end{aligned} \tag{24}$$

Equation (17) is rewritten using above Helmholtz free energy and incompressible invariants as follows:

$$\begin{aligned}\mu_g\dot{\mathbf{C}}_g^v =& \left(J_g^e\right)^{-2/3}\left(\mathbf{C}_g^v\right)^{-1}\mathbf{C}_g^{ev}\left\{\left(C_{10,g}^e+\bar{I}_g^eC_{01,g}^e\right)\mathbf{I}-\left(J_g^e\right)^{-2/3}C_{01,g}^e\left(\mathbf{C}_g^v\right)^{-1}\mathbf{C}_g^{ev}\right\}\left(\mathbf{C}_g^v\right)^{-1}\\ &+\left\{-\frac{1}{3}\left(\bar{I}_g^eC_{10,g}^e+2\bar{II}_g^eC_{01,g}^e\right)+\frac{1}{2}\kappa_g^eJ_g^e\left(J_g^e-1\right)\right\}\left(\mathbf{C}_g^v\right)^{-1}\\ &-\left\{\left(J_g^v\right)^{-2/3}\left(C_{10,g}^v+\bar{I}_g^vC_{01,g}^v\right)\mathbf{I}-\left(J_g^v\right)^{-4/3}C_{01,g}^v\mathbf{C}_g^v\right\}\\ &-\left\{-\frac{1}{3}\left(\bar{I}_g^vC_{10,g}^v+2\bar{II}_g^vC_{01,g}^v\right)+\frac{1}{2}\kappa_g^vJ_g^v\left(J_g^v-1\right)\right\}\left(\mathbf{C}_g^v\right)^{-1}\end{aligned} \tag{25}$$

where $\mathbf{C}_g^{ev}=\left(\mathbf{F}_g^e\mathbf{F}_g^v\right)^T\mathbf{F}_g^e\mathbf{F}_g^v$. This equation solves $\mathbf{C}_g^v$ with the total deformation ($\mathbf{C}$) given, provided that viscoplastic deformation ($\mathbf{F}_g^p$) and shape memory strain ($\mathbf{F}_g^s$) are given. These two deformation gradients are described separately using another constitutive laws as follows.

To describe the viscoplastic element, Perzyna model (Perzyna, 1966) was used:

$$\dot{\mathbf{F}}_g^p=\frac{1}{\mu_g^p}\langle f\rangle\frac{\partial f}{\partial\mathbf{P}_g} \tag{26}$$

In here, the yield function is

$$f\left(\boldsymbol{\sigma}_g,\alpha^p\left(t\right)\right)=\sqrt{\frac{3}{2}\boldsymbol{\sigma}_g^d:\boldsymbol{\sigma}_g^d}-\left\{\sigma^Y+E^p\left(\alpha^p\left(t\right)\right)^2\right\} \tag{27}$$

where $\boldsymbol{\sigma}_g^d=\boldsymbol{\sigma}_g-tr\left(\boldsymbol{\sigma}_g\right)/3\mathbf{I}$ is the deviatoric stress of the Cauchy stress and $\alpha^p\left(t\right)=\int_0^t\dot{\varepsilon}^pd\tau$ is the equivalent viscoplastic strain expressed with respect to the effective plastic strain $\dot{\varepsilon}^p=\sqrt{2/3}\left\|\dot{\mathbf{F}}_g^p\left(\mathbf{F}_g^p\right)^{-1}\right\|$ (Yang et al., 2006). σ^Y, E^p, and μ_g^p are the yield strength, the hardening modulus, and the viscosity of the dashpot, respectively.

2.2.3 Empirical constitutive equation for shape memory strain

Shape memory strain was introduced to represent the strain, which is necessary for proper modeling of the shape memory effect, particularly a temporarily fixed shape. Consider the thermo-mechanical cycling behavior of SMP to understand the shape memory strain and further to gain insight into its constitutive description. During the stretching step of the thermomechanical cyclic test at high temperature (step 1 in Fig. 6(a) and (b)), the shape memory strain is generated and remained until heating is applied (step 4 in Fig. 6(a) and (b)). During the cooling step (step 2 in Fig. 6(a) and (b)), the stress relaxation occurs because the shape memory strain occupies the greatest portion of the extension, as shown in the third column in Fig. 6(a). After the stress release (step 3 in Fig. 6(a) and (b)), the shape of the SMP is nearly fixed because the mechanical strain applied during the step 1 is stored as the shape memory strain (a kind of non-mechanical strains) as illustrated in the fourth column in Fig. 6(a). Finally, when the SMP is heated (step 4 in Fig. 6(a) and (b)), i.e., the rubbery phase is the dominant phase, regaining the entropic elasticity and returning to its original shape in a stress-free state. At this step, the shape memory strains go extinction. The physical source of the remaining shape memory strain just after the unloading step is the internal microstructure of SMP. As the temperature decreases below T_{tr}, the polymer chains in the SMPs lose their mobility due to the reduced free volume (frozen effect) and thus lose the entropic elasticity. This results in the residual strain (shape memory strain) despite external load removal. The shape memory strain corresponds to the residual strain, i.e., the fraction of the total deformation that is not released upon unloading.

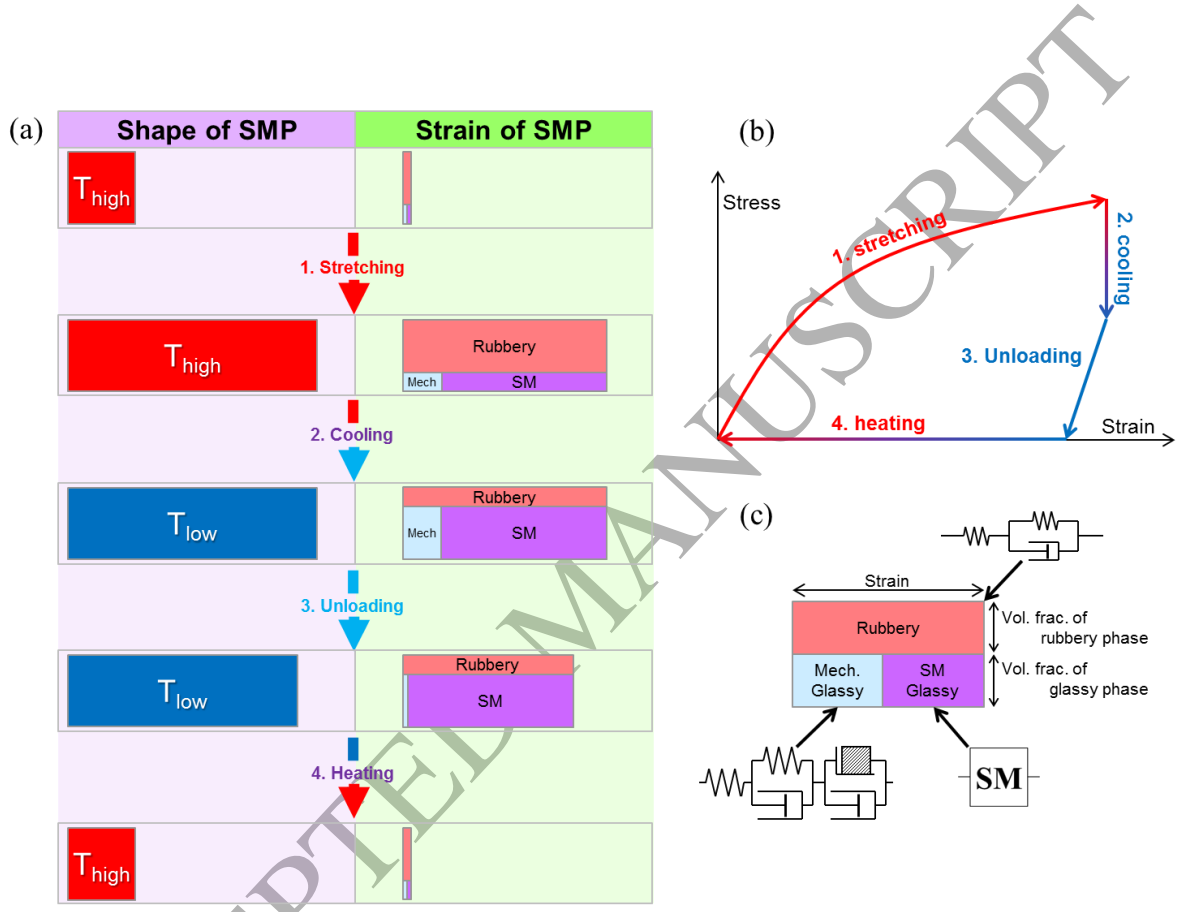

Fig. 6. Schematic description of shape memory strain. (a) Generation and extinction of the shape memory strain during the thermo-mechanical cycling and its contribution to the shape memory behavior of the SMP. (b) Stress–strain curve corresponding to the thermomechanical steps in (a). (c) Schematic drawing of the strain composition. The horizontal and vertical lines represent the amount of strain and the volume fraction of each phase, respectively. 'Mech. Glassy' represents the strain of the glassy phase, while 'SM Glassy' means the shape memory strain generated in the glassy phase.

Considering the shape memory strains generated or disappeared in the thermo-mechanical cyclic behavior of SMP, we assumed that the rate of the shape memory strain (E_g^s) is proportional to the volume fraction of the rubbery phase ξ_r and a function of actual total deformation, i.e.,

$$\frac{dE_g^s}{dt} \propto \xi_r f\left(E, E_g^s\right) \tag{28}$$

where E represents the total strain. The actual form of $f\left(E, E_g^s\right)$ should be prescribed explicitly for obtaining the deformation gradient of the shape memory strains. For ideal SMPs, the amount of shape memory strain would exponentially converge to total strain itself, but practically, it approaches a certain limit of total strain. Consequently, a simple tensorial form was used in this study as follows:

$$\frac{d\mathbf{E}_g^s}{dt} = \begin{cases} \alpha\xi_r\left(-\mathbf{E}_g^s + \beta\mathbf{E}\right) & \text{for} \quad \left|\beta E_{ij}\right| > \left|E_{g,ij}^s\right| \\ \alpha\xi_r\left(-\mathbf{E}_g^s + \mathbf{E}\right) & \text{for} \quad \left|E_{ij}\right| < \left|E_{g,ij}^s\right| \end{cases} \tag{29}$$

where α is a constant to represent the formation rate of the shape memory strain and β (always less than one) is a fraction of the total strain that the shape memory strain can take, i.e., the maximum shape memory strain is $\beta\mathbf{E}$. $\left|\beta E_{ij}\right| > \left|E_{g,ij}^s\right|$ means applying deformation while $\left|E_{ij}\right| < \left|E_{g,ij}^s\right|$ represents releasing deformation. The signs of absolute value of these expressions are to consider not only extension but also compression. The solution of Equation (29) can be obtained using a direct solver for ordinary differential equation (e.g., MUMPS(Amestoy et al., 2006) or PARDISO(Schenk and Gärtner, 2004)). Next, the deformation gradient of the shape memory strain is obtained using its rotationless assumption as follows.

The stretch tensor of the shape memory strain element can be written as follows:

$$\mathbf{U}_0^s = \sum_{i=1}^{3} \lambda_i^s \left(\mathbf{M}_i^s \otimes \mathbf{M}_i^s \right) \tag{30}$$

where $\left(\lambda_i^s\right)^2$ represents the principal stretches, and $\mathbf{M}_i^s$ are the principal directions of $\mathbf{C}_0^s$, the right Cauchy-Green tensor of the shape memory strain. Here, $\mathbf{C}_0^s$ is provided in terms of the Lagrange strain ($\mathbf{E}_g^s$) given by Equation (29), i.e., $\mathbf{C}_0^s = 2\mathbf{E}_g^s + \mathbf{I}$. A more practical form of $\mathbf{U}_g^s$ is given by

$$\mathbf{U}_g^s = \sum_{i=1}^{3} \frac{\lambda_i^s}{\left(J^s\right)^{1/3}} \left(\mathbf{M}_i^s \otimes \mathbf{M}_i^s \right) \tag{31}$$

where $J^s = \prod_{i=1}^{3} \lambda_i^s$ is the volume change of the shape memory strain. The reason that this is more practical or that the factor $1/\left(J^s\right)^{1/3}$ is introduced is for the incompressibility of the shape memory strain component. Finally, the deformation gradient of the shape memory strain part can be expressed as follows:

$$\begin{aligned} \mathbf{F}_g^s &= \mathbf{R}_g^s \mathbf{U}_g^s = \mathbf{U}_g^s \\ &= \sum_{i=1}^{3} \frac{\lambda_i^s}{\left(J^s\right)^{1/3}} \left(\mathbf{M}_i^s \otimes \mathbf{M}_i^s \right) \end{aligned} \tag{32}$$

Note that the rotationless ($\mathbf{R}_g^s = \mathbf{I}$) is assumed.

2.3 Calculation of stresses

Total stress is expressed as volumetric summation of stresses of rubbery and glassy phase, as written in Equation (2). First, Equation (14) is retrieved to calculate the stress of the rubbery phase. Equation (14) gives

$$\begin{aligned}\mathbf{S}_r &= 2\frac{\partial \psi_r^e}{\partial \mathbf{C}} \\ &= 2\frac{\partial \psi_r^e}{\partial I_r^e}\frac{\partial I_r^e}{\partial \mathbf{C}} + 2\frac{\partial \psi_r^e}{\partial II_r^e}\frac{\partial II_r^e}{\partial \mathbf{C}} + 2\frac{\partial \psi_r^e}{\partial III_r^e}\frac{\partial III_r^e}{\partial \mathbf{C}}\end{aligned} \tag{33}$$

Using Equation (6) and incompressible invariants, the second Piola-Kirchhoff stress of the rubbery phase is given by

$$\begin{aligned}\mathbf{S}_r = {} & 2\left(J_r^e\right)^{-2/3}\left[\left(C_{10,r}^e + \bar{I}_r^e C_{10,r}^e\right)\mathbf{I} - \left(J_r^e\right)^{-2/3} C_{01,r}^e \left(\mathbf{C}_r^v\right)^{-1}\mathbf{C}\right]\left(\mathbf{C}_r^v\right)^{-1} \\ & +2\left\{-\frac{1}{3}\left(\bar{I}_r^e C_{10,r}^e + 2\bar{II}_r^e C_{01,r}^e\right) + \frac{1}{2}\kappa_r^e J_r^e\left(J_r^e - 1\right)\right\}\mathbf{C}^{-T}\end{aligned} \tag{34}$$

This equation calculates the stress of the rubbery phase using the given total deformation ($\mathbf{C}$) and viscoelastic deformation ($\mathbf{C}_r^v$) calculated by Equation (23).

Similarly, Equation (16) gives,

$$\begin{aligned}\mathbf{S}_g &= 2\frac{\partial \psi_g^e}{\partial \mathbf{C}} \\ &= 2\frac{\partial \psi_g^e}{\partial I_g^e}\frac{\partial I_g^e}{\partial \mathbf{C}} + 2\frac{\partial \psi_g^e}{\partial II_g^e}\frac{\partial II_g^e}{\partial \mathbf{C}} + 2\frac{\partial \psi_g^e}{\partial III_g^e}\frac{\partial III_g^e}{\partial \mathbf{C}}\end{aligned} \tag{35}$$

Also using Equation (6) and incompressible invariants, the second Piola-Kirchhoff stress of the glassy phase is given by

$$\begin{aligned}\mathbf{S}_g = {} & 2\left(J_g^e\right)^{-2/3}\left(\mathbf{F}_g^a\right)^{-1}\left[\left(C_{10,g}^e + \bar{I}_g^e C_{10,g}^e\right)\mathbf{I} - \left(J_g^e\right)^{-2/3} C_{01,g}^e \left(\mathbf{C}_g^v\right)^{-1}\mathbf{C}_g^{ev}\right]\left(\mathbf{C}_g^v\right)^{-1}\left(\mathbf{F}_g^a\right)^{-T} \\ & +2\left\{-\frac{1}{3}\left(\bar{I}_g^e C_{10,g}^e + 2\bar{II}_g^e C_{01,g}^e\right) + \frac{1}{2}\kappa_g^e J_g^e\left(J_g^e - 1\right)\right\}\mathbf{C}^{-T}\end{aligned} \tag{36}$$

where $\mathbf{F}_g^a = \mathbf{F}_g^p\mathbf{F}_g^s$ and $\mathbf{C}_g^{ev} = \left(\mathbf{F}_g^e\mathbf{F}_g^v\right)^T\mathbf{F}_g^e\mathbf{F}_g^v = \left(\mathbf{F}_g^a\right)^{-T}\mathbf{C}\left(\mathbf{F}_g^a\right)^{-1}$. This is the final form of the stress of the glassy phase calculated using the given total deformation ($\mathbf{C}$), viscoelastic deformation ($\mathbf{C}_g^v$) calculated by Equation (25), viscoplastic deformation ($\mathbf{F}_g^p$) calculated by Equation (26), and shape memory strain ($\mathbf{F}_g^s$) solved by Equation (32).

2.4 Summary of the model

Final form of the constitutive equation is given by Equation (2), (34), and (36), in which there are many material parameters, which should be determined from some experimental. In this section, the material parameters of an SMP (which will be described in Section 3.1), which were determined using a procedure in Appendix B, are listed in Table 1.

Table 1. Material coefficients of the constitutive equation of an SMP.

	$T_{tr} = 44.3℃$	Transition temperature
Volume fraction (See Eqn (3))	$b = 1.30$ $c = 0.137℃^{-1}$ $d = 0.136$	Fitting parameters
Rubbery phase (See Eqns (23) and (34))	$C^e_{10,r} = 0.02\text{MPa}$ $C^e_{01,r} = 0.30\text{MPa}$	Spring constants of the first spring
	$\kappa^e_r = 90MPa$	Bulk modulus of the first spring
	$C^v_{10,r} = 0.55\text{MPa}$ $C^v_{01,r} = 0.50\text{MPa}$	Spring constants of the second spring
	$\kappa^v_r = 90MPa$	Bulk modulus of the second spring
	$\mu_r = 0.336GPa \cdot s$	Viscosity of the dashpot
Glassy phase (See Eqns (25) and (36))	$C^e_{10,g} = 0$ $C^e_{01,g} = 20\text{MPa}$	Spring constants of the first spring
	$\kappa^e_g = 600MPa$	Bulk modulus of the first spring
	$C^v_{10,g} = 0$ $C^v_{01,g} = 13MPa$	Spring constants of the second spring
	$\kappa^v_g = 600MPa$	Bulk modulus of the second spring
	$\mu_g = 0.7GPa \cdot s$	Viscosity of the dashpot parallel to the second spring
Viscoplasticity (See Eqns (26) and (27))	$\sigma^Y = 3MPa$	Yield strength
	$E^p = 18MPa$	Hardening modulus
	$\mu^p_g = 16GPa \cdot s$	Viscosity of the dashpot in the viscoplastic element
Shape memory strain (See Eqns (29) and (32))	$\alpha = 0.72s^{-1}$	Formation rate of the shape memory strain
	$\beta = 0.987$	Ratio of shape memory strain to total deformation

3. Experimental

3.1 Material preparations

A poly(cyclooctene) (PCO) SMP was synthesized following a literature procedure (Liu et al., 2002): (i) PCO was dissolved in tetrahydrofuran (THF) to form PCO solution at 80 °C. (ii) After 24 hours, dicumyl peroxide (DCP) was added to the PCO-THF solution. The ratio of DCP to PCO was 1 wt%. (iii) The solution was placed in a fume hood to vaporize THF for 24 hours at room temperature. (iv) Next, the solution was placed in a vacuum oven for 1 hour at 80 °C. (v) The sample was then cut to appropriate size for each mechanical test. (vi) The sample was pre-heated for 5 minutes at 80 °C and then finally heated to 170 °C and held for 30 minutes. Thermogram of the PCO SMP sample was obtained using differential scanning calorimetry (DSC), from which the temperature range of the PCO for shape memory behavior was determined to be from 30 to 60 °C (see Appendix C for details).

3.2 Uniaxial thermo-mechanical shape memory tests

Using PCO film in 1 × 5 × 0.12 cm size, the shape memory test was carried out using a four-step test: (i) extension of the sample by 200% at a rate of 33.6 mm/min at 60 °C; (ii) stress relaxation while maintaining strain during cool down to 30 °C at a rate of 21 °C/min; (iii) 300 seconds of unloading to zero stress; and (iv) heating to 60 °C at a rate of 20 °C/min under zero load. The stress was measured under the prescribed strain conditions during steps (i) and (ii), while the strain was measured under the prescribed stress conditions during steps (iii) and (iv).

3.3 Punching test

Multi-dimensional deformation behavior of the SMP was evaluated in an environmental chamber to validate the developed constitutive model and its implementation in finite element

software. A PCO sheet was prepared with dimensions of 9 × 9 × 0.12 cm (length × width × thickness). With all edges of the PCO sheet clamped, the center region of the sample was punched to certain heights (30, 37.5, and 45 cm) using a rigid spherical tool with a radius of 0.65 cm at 60 °C (Fig. 7(a)). The punch was held in place while lowering the temperature to 30 °C at a rate of 21 °C/min. The punch was then retracted, allowing the sheet to relax. The temperature was then increased to 60 °C, and the applied force and deformation of the sheet were recorded by the testing machine. To measure the strains along *X*-, *Y*-, and diagonal directions, grid patterns were introduced on the surface of the SMP sheet, as shown in Fig. 7(b).

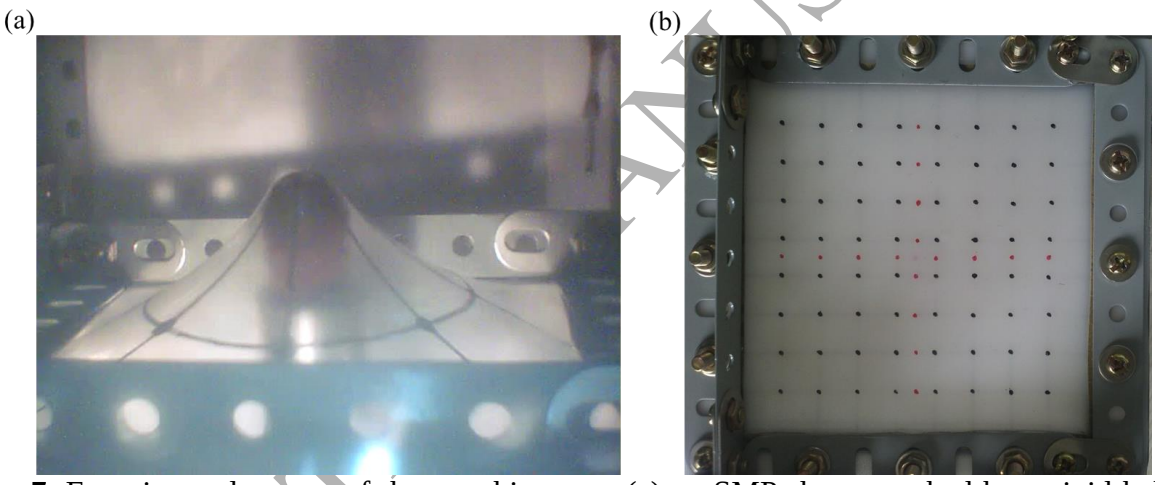

Fig. 7. Experimental scenes of the punching test: (a) an SMP sheet punched by a rigid ball and (b) grids on the sheet surface to measure the strain.

4. Results and discussions

Two boundary value problems were chosen to validate the current constitutive model. First, uniaxial tensile tests, including the thermo-mechanical cyclic test of SMPs of Section 3.2, were simulated and compared to experimental data. Next, the 3D deformation behavior of SMPs from Section 3.3 was simulated using the constitutive model. All simulations were carried out using COMSOL™ software, into which the following virtual work was input in weak form:

$$\int_{V_0} \mathbf{S} : \delta\mathbf{E} dV_0 = \int_{A_0} \mathbf{T} \cdot \delta\mathbf{u} dA_0 + \int_{V_0} \mathbf{f} \cdot \delta\mathbf{u} dV_0 \tag{37}$$

where $\mathbf{T}$ and $\mathbf{f}$ are external surface traction and volumetric force, respectively, and dA_0 and dV_0 represent the area and volume element, respectively. Ordinary differential equations such as Equations (23), (25), (26), and (29) were solved by domain ODE solver.

4.1 Uniaxial tensile behavior of SMPs

An SMP sheet with the dimensions 1 × 3 × 0.12 cm (length × width × thickness) was used in the thermo-mechanical cyclic tensile test described in Section 3.2. The specimen was modeled using tetrahedral finite elements (7,177 elements). The nodes on the left cross-section [perpendicular to the loading axis (*x*-axis)] were all fixed ($u = v = w = 0$), while the displacement of nodes on the opposite side were prescribed by $u = u_{input}$ and $v = w = 0$ (see Fig. 8).

Fig. 9 presents the results of the thermo-mechanical cyclic test. As evident from these results, the calculated results using the finite element method are within good agreement with experimental results. We observed a peak of the 3D modeling curve at time 900 s in Fig. 9(b).

This can be explained by the thermo-mechanical cycle steps and our parallel model. The heating increased the volume fraction of the rubbery phase, inducing the rubbery phase (already stretched in the first step) to shrink. Due to the isostrain approach (i.e., a parallel combination of the rubbery and glassy phases) in this study, the glassy phase became compressed (in particular, hyperelastic spring and viscoelastic element of glassy phase have negative strains) (see Fig. 10(a) for strain profiles). On the other hand, stresses on rubbery and glassy phases became positive and negative, respectively, to make the total stress zero. Note that the recovery of the SMP occurred under zero force. This continued until about $t = 900$ s. After that, smaller tensile and compressive stresses were applied to the rubbery and glassy phases, respectively. At $t = 908$ s, these two stresses became all zero (see Fig. 10(b)). Further decreased shape memory strain induced positive and negative stress on the glassy and rubbery, respectively, even though the total stress became zero. This stress configuration brought about unstable and transitive strain increase. Note that Fig. 9(b) shows the variation of the engineering strain for 1351 s. Further calculation, e.g., up to 4500 s, confirmed complete recovery of total strain (i.e., zero strain) for 3D modeling case. The shape memory polymer used in this research did not recover its original shape, i.e., the unrecovered strain and recovery rate at 4500 s was about 11.1% and 94.5%, respectively. Fig. 9(d) shows the simulated deformed shapes during the cyclic test, demonstrating that the shape memory strain is a proper quantity for simulating the shape memory behavior of SMPs. The distribution of the shape memory strain, $\left\|\mathbf{E}_g^s\right\|$, is shown in Fig. 11. In this figure, $t = 112$ s indicates the time to maximum strain at $T = T_h$, while $t = 511$ s is the time just prior to unloading, i.e., the last moment for producing shape memory strain. The distributions of the shape memory strain between the two time steps are similar, implying that the shape memory strain at $T = T_h$ was produced at an early stage, i.e., the shape memory strain was induced almost immediately up-

on deformation. Fig. 11 also shows that the shape memory strain was generated near the center of the sample rather than in the constrained region, which is consistent with the assumption that the shape memory strain is proportional to the total deformation, because larger deformation occurs in the central region than at the edges.

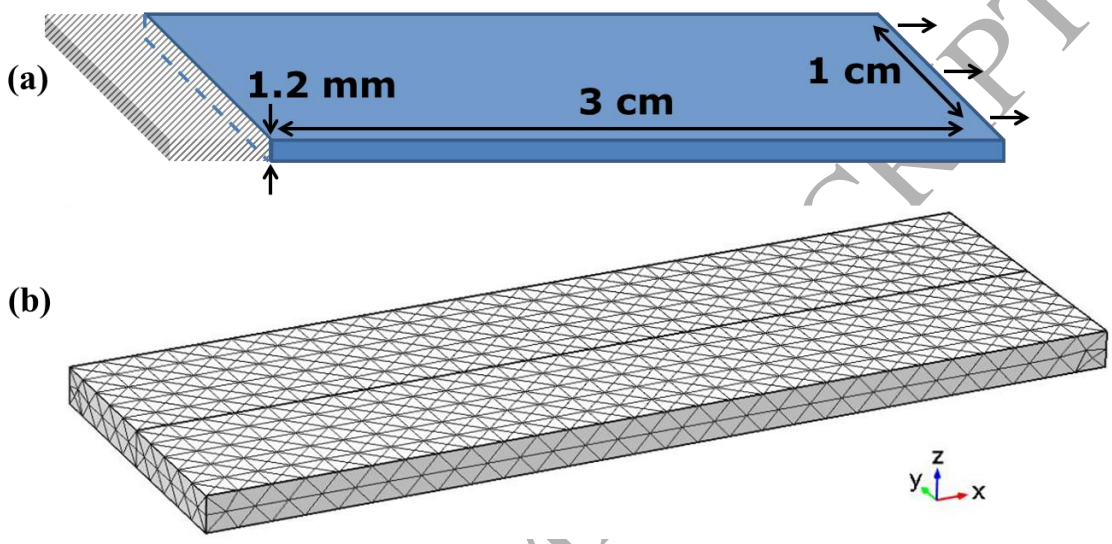

Fig. 8. (a) Geometry and (b) mesh configuration of a rectangular SMP sample.

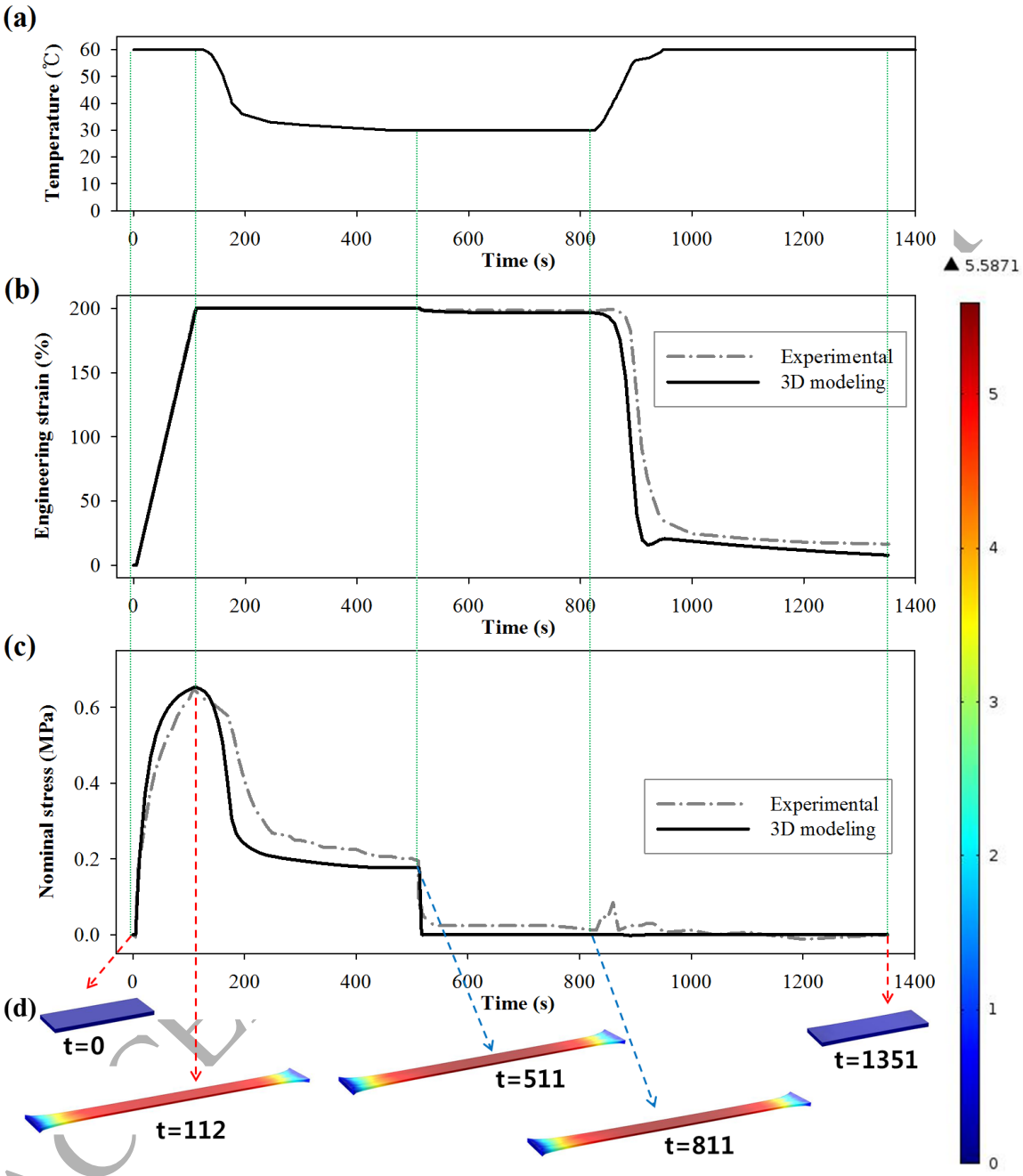

Fig. 9. Experimental and modeling results of the thermo-mechanical cyclic test: (a) input temperature, (b) strain-time, (c) stress-time, and (d) 3D shape change over time. The color indicates the magnitude of the shape memory strain, i.e., $\left\|\mathbf{E}_g^s\right\|$.

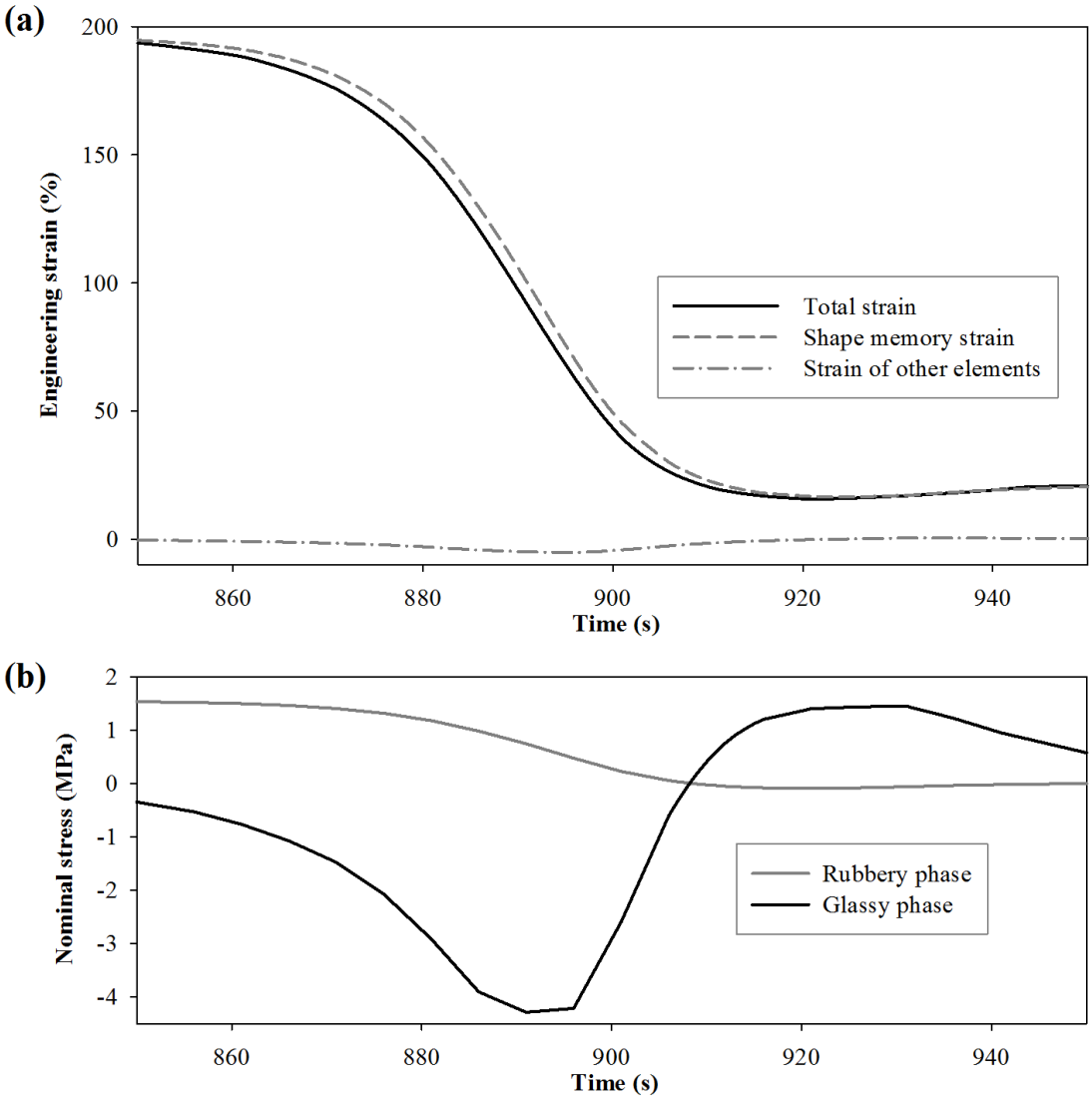

Fig. 10. Evolution of (a) strain and (b) stress during the thermo-mechanical cyclic test.

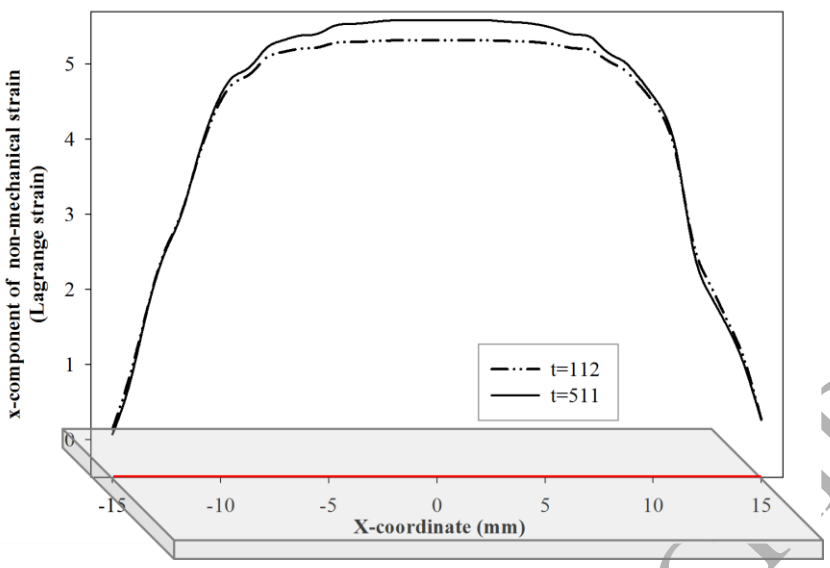

Fig. 11. Distribution of the *x*-component of the shape memory strain along the central line (from [-15 mm, 0, 0] to [15 mm, 0, 0] in the material coordinate).

4.2 Punching simulation

An SMP sheet with dimensions 9 × 9 × 0.12 cm (length × width × thickness) was used for the punching simulation, as shown in Fig. 12. The total number of the tetrahedral mesh was 18,652. As boundary conditions, all nodes on four edges were fixed ($u = v = w = 0$). A spherical rigid ball with a radius of 0.65 cm was used to press the sheet upward at the center position. The simulation followed the same procedure described in Section 3.3.

Fig. 13(b) shows the displacement of the center point of the sheet in the *z*-direction. The *z*-displacement of the center point before $t = 511$ s was determined by punch movement. Simulated fixities of the sheet were larger than the experimental fixity such that the sample almost recovered its original shape. The experimental results did not indicate complete recovery, leaving about 10 mm displacement unrecovered. This discrepancy in displacement seems large, but actual unrecovered in-plane deformations were small (2%). This small, unrecovered deformation caused a large unrecovered *z*-displacement of the center point. The overall

tendency of the simulated fixities and recovery were well matched with experimental results. As indicated in Fig. 13(c), which presents deformed shapes of the sheet in the punching simulation, the current constitutive model is adequate for simulating the mechanical behavior of the SMP. The overall deformed shape was well matched by the experimental shape shown in Fig. 7(a).

The simulation results were quantitatively compared by obtaining the strain of the sheet at a specified time. Fig. 14(a)–(c) shows the strain along the *X*-, *Y*-, and diagonal axes at $t = 511$ s. In general, the simulated (calculated) strains agreed with experimentally determined ones, although small deviations were observed. For example, the simulated strains from the origin ($X = 0$) to $X = 15$ mm were larger than those obtained experimentally. The differences might be attributable to friction between the sheet sample and the sphere punch in the experiment, because the friction between the sheet and tools was not taken into account in the simulation. Fig. 14(d) shows the distribution of the shape memory strain ($\left\|\mathbf{E}_g^s\right\|$) along the *X*-axis. At a punching displacement of 30 mm, the total deformation was small, and the $\left\|\mathbf{E}_g^s\right\|$ distribution did not vary significantly. As the punching displacement increased, however, a dramatic change in the distribution was observed, in particular at a punching displacement of 45 mm, where a large shape memory strain appeared concentrated around $X = 4$ mm and $X = 10$ mm, implying that the total deformations of the sheet were local maxima at these locations. Then, $\left\|\mathbf{E}_g^s\right\|$ decreased toward the center of the sheet ($X = 0$), because biaxial deformation in this region [$\det\left(\mathbf{F}_g^s\right)$] was close to identity. Similar to the uniaxial test case, the shape memory strain was induced immediately upon deformation of the sample before $t = 112$ s.

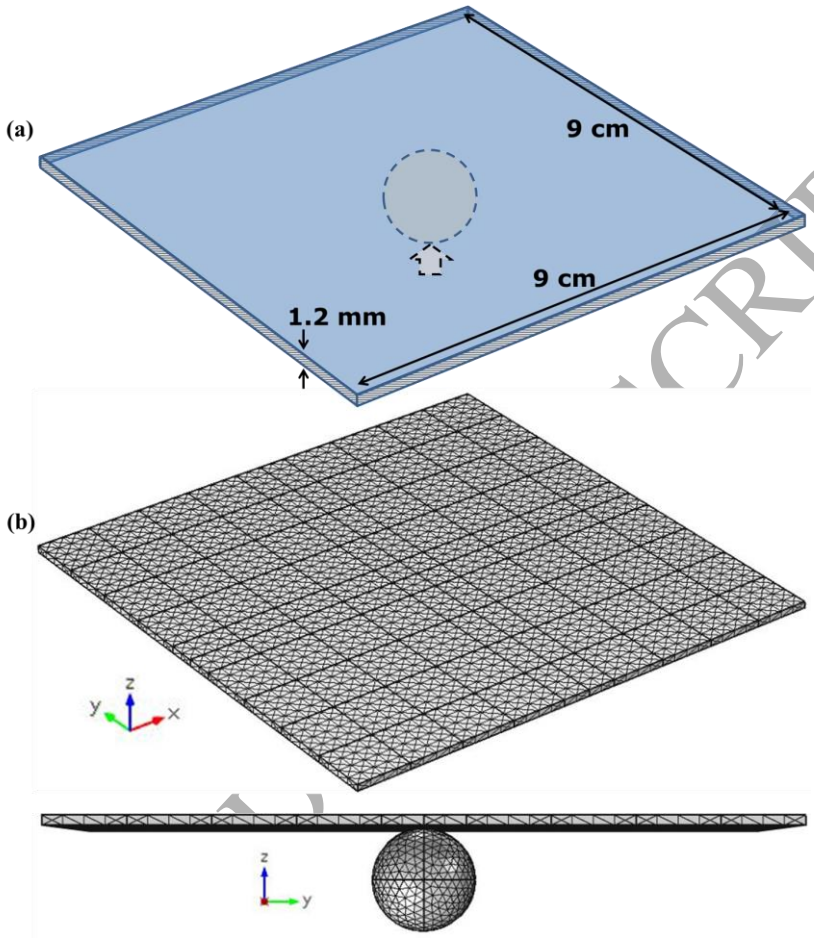

Fig. 12. (a) Geometry and (b) mesh configuration of an SMP sheet and a punch.

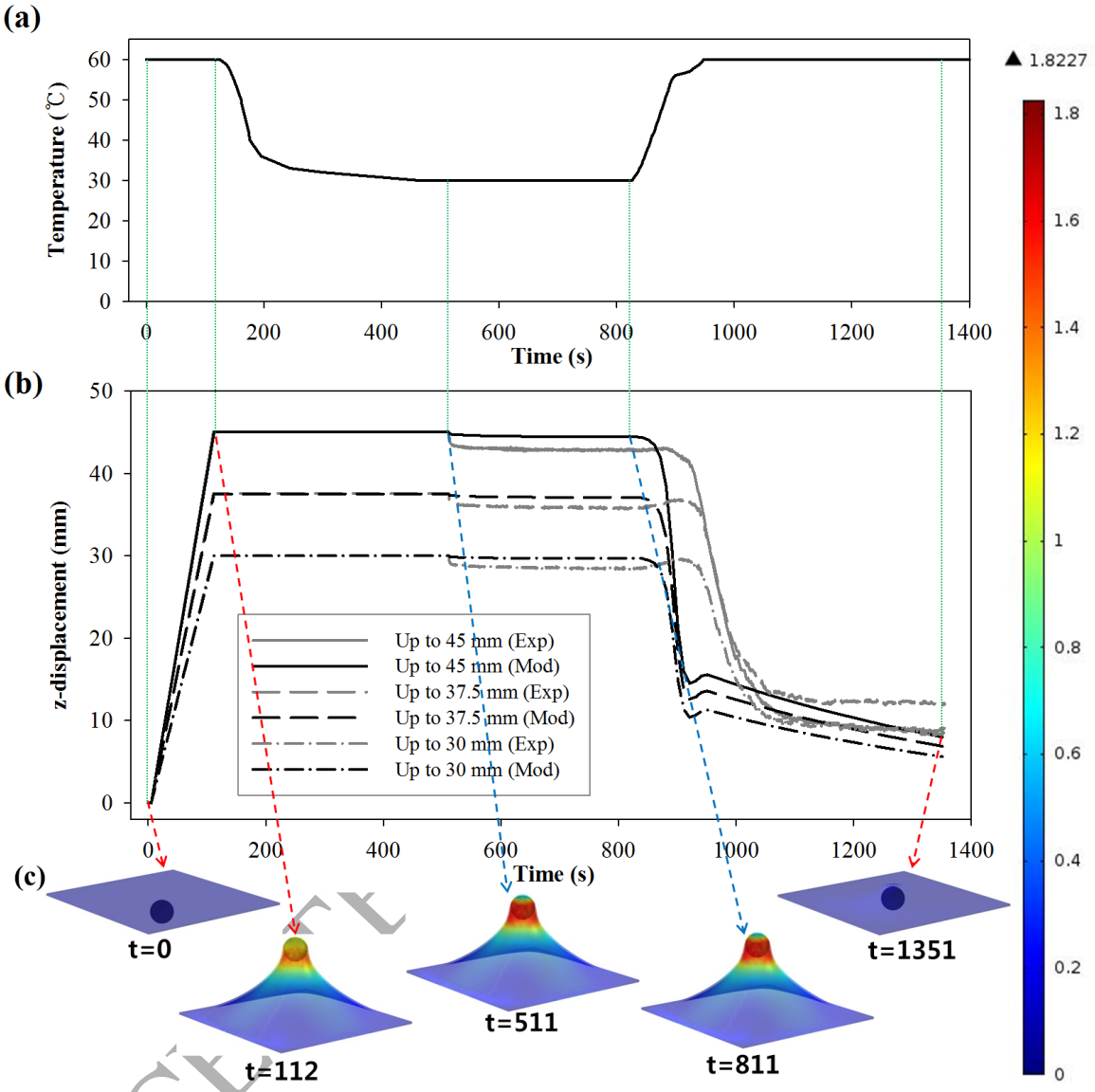

Fig. 13. Experimental and modeling results of the punching test: (a) temperature input, (b) *z*-directional displacement of the center point in the sheet, and (c) 3D shape changes of the SMP sheet with time when maximum *z*-displacement of the punch was 45 mm. The color indicates the magnitude of shape memory strain, i.e., $\left\|\mathbf{E}_g^s\right\|$.

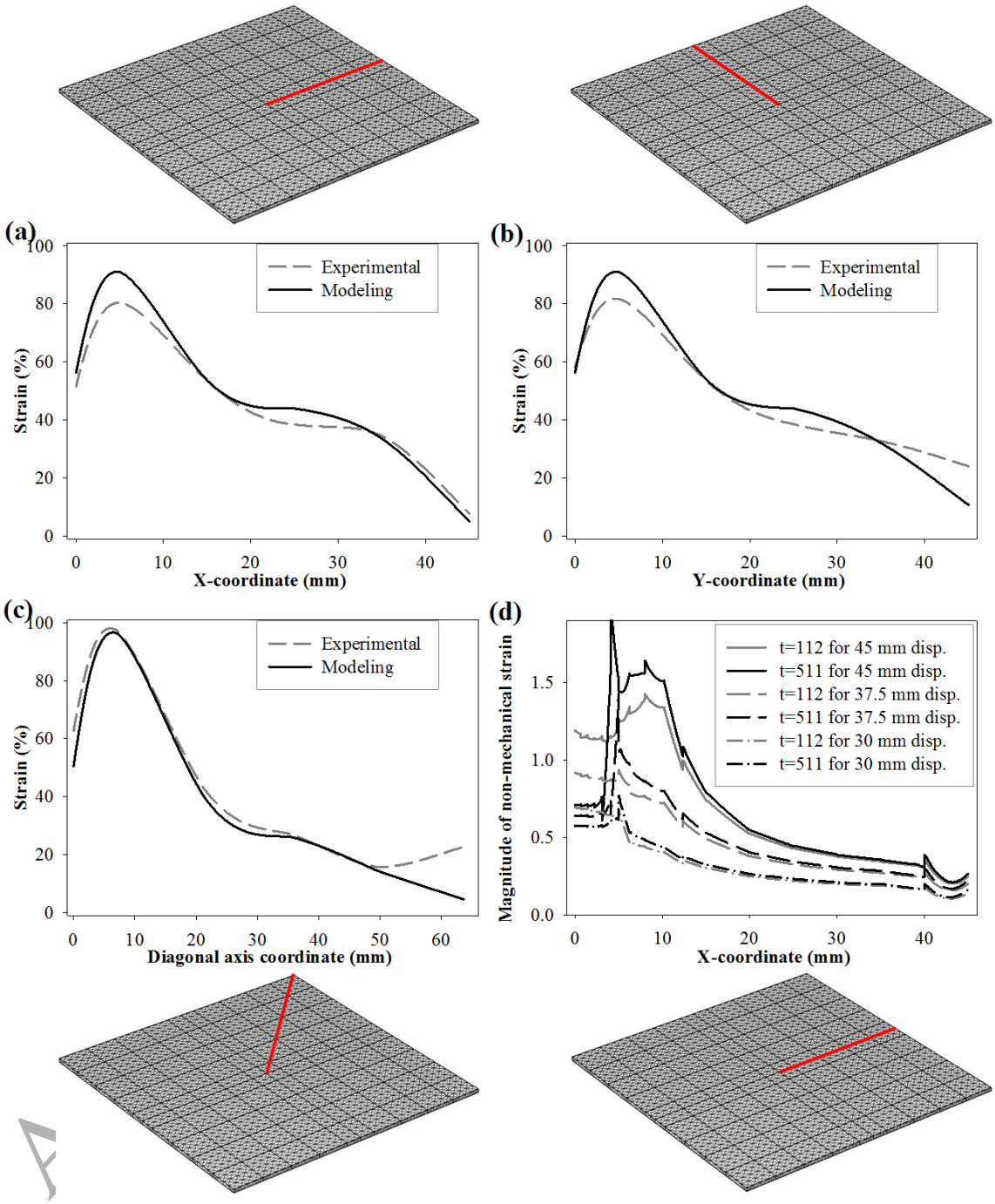

Fig. 14. Quantitative comparisons of simulation results with experiments: (a) Strain along the *X*-, (b) *Y*-, and (c) diagonal axes at $t = 511$ s at a punching displacement of 45 mm and (d) evolution of shape memory strains along the *X*- axis.

5. Conclusion

A 3D constitutive equation for SMPs was developed using a phenomenological two-phase (rubbery and glassy) model. The shape memory strain concept, which was determined by the principal axes and stretches of the total deformation, was introduced to simulate the shape memory behavior of SMPs. The material parameters of SMPs for the 3D constitutive equation were determined by deriving reduced 1D constitutive equations, calculating the thermo-mechanical deformation behavior of 1D SMPs, and comparing the calculated results with experimental results. The constitutive equation was validated by simulating the deformation behavior of an SMP sheet undergoing a series of thermo-mechanical deformations, including punching at high temperature, releasing to temporary shape at low temperature, and finally restoring to the permanent shape at high temperature. Comparison of simulated results with experiments demonstrated that the current constitutive equation can properly capture the multi-dimensional deformation behavior of SMPs.

Acknowledgement

This work was supported by the Mid-career Researcher Program through the National Research Foundation of Korea (NRF) grant funded by the Korean Government (MSIP) (2013R1A2A2A01067717).

Appendix A. Volume fraction of the glassy phase

A relaxation test was carried out to obtain the volume fraction of PCO according to temperature. The PCO sample was stretched to 200% at 30 °C. The applied strain was maintained for 1000 seconds for sufficient relaxation. The temperature was then increased to 60 °C at a rate of 1.00 °C/min, during which the stress evolution was measured.

The nominal stress at $T = T_l$ is given by the following equation:

$$P(T_l) = \xi_g P_g \quad \text{with} \quad \xi_g = 1 \tag{A. 1}$$

Similarly, at $T = T_h$, the stress is

$$P(T_h) = \xi_r P_r \quad \text{with} \quad \xi_r = 1 \tag{A. 2}$$

At the intermediate temperature, Equation (2) can be rewritten as

$$\begin{aligned} P &= (1-\xi_g) P(T_h) + \xi_g P(T_l) \\ &= P(T_h) + \xi_g \{P(T_l) - P(T_h)\} \end{aligned} \tag{A. 3}$$

or

$$\xi_g = \frac{P - P(T_h)}{P(T_l) - P(T_h)} \tag{A. 4}$$

The above equations show how $\xi_g(T)$ can be obtained from the experimental data for $P(T)$. An appropriate regression function for ξ_g can be obtained using the stress–temperature curve [see Fig. A.1] as follows:

$$\xi_g = \begin{cases} 1 & 1 < \xi_g^0 \\ \xi_g^0 & 0 \le \xi_g^0 \le 1 \\ 0 & \xi_g^0 < 0 \end{cases} \quad \text{with} \quad \xi_g^0 = \frac{b}{1 + \exp\left(c\left(T - T_{tr}\right)\right)} - d \tag{A. 5}$$

where $b = 1.30$, $c = 0.137$ °C^{-1}, $T_{tr} = 44.3$ °C, and $d = 0.136$. This is Equation (3) and ξ_r

is obtained just by $1-\xi_g$.

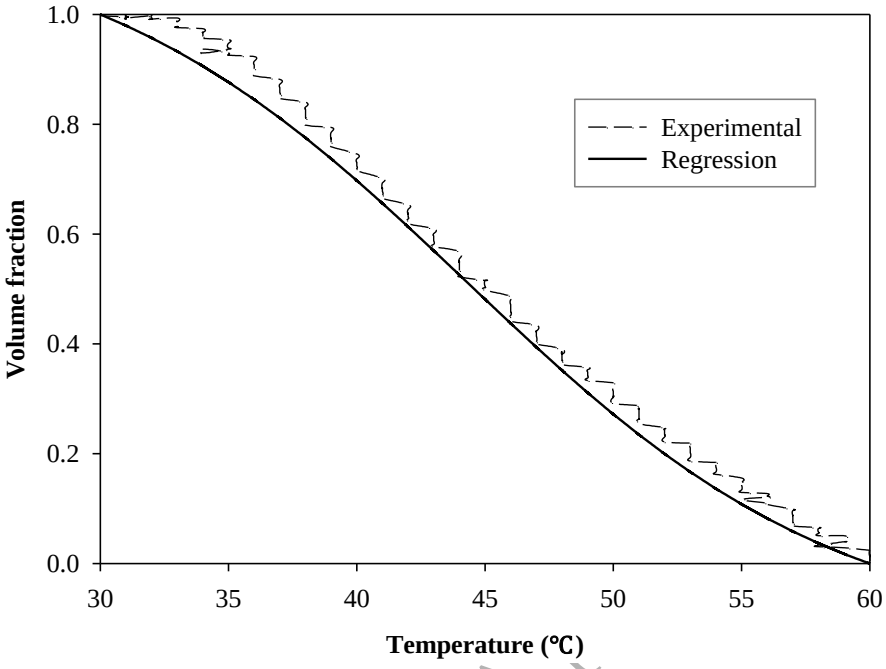

Fig. A.1. Variation of the volume fraction (ξ_g) of the glass phase with increasing temperature.

Appendix B. Obtaining material parameters of the glassy and rubbery phases

Material parameters for this model were determined via trial and error by fitting the constitutive equations to the experimental data from Isothermal uniaxial tests (below section) and thermo-mechanical shape memory test (Section 3.2). For these operations, the 3D constitutive equations were reduced to a 1D form by assuming uniaxial extension.

B.1. Isothermal uniaxial tests

Isothermal uniaxial tests were carried out to determine the material parameters in the constitutive model. A PCO flim was prepared with dimensions of 1 × 5 × 0.12 cm (length × width × thickness) with a gauge length of 3 cm. An isothermal uniaxial test was performed at 60 °C to characterize the rubbery phase of the SMP. The SMP sample was extended 200% at

a rate of 240 mm/min. The strain was then fixed for 1000 seconds, and the stress was measured. The sample was unloaded, and the strain was measured. An additional isothermal test was performed at 30 °C. The sample was extended 200% at a rate of 0.35 mm/min. The strain was then fixed for 3000 seconds, during which time the stress was measured. Finally, the strain was measured again after sample unloading.

B.2. 1D form of the model of the glassy phase

If the glassy phase is incompressible, $\mathbf{F}$, $\mathbf{F}_g^e$, $\mathbf{F}_g^v$, $\mathbf{F}_g^p$, and $\mathbf{F}_g^s$ can be written as follows:

$$\mathbf{F}_j^k = \begin{bmatrix} \lambda_j^k & 0 & 0 \\ 0 & 1/\sqrt{\lambda_j^k} & 0 \\ 0 & 0 & 1/\sqrt{\lambda_j^k} \end{bmatrix} \Rightarrow \mathbf{C}_j^k = \begin{bmatrix} \left(\lambda_j^k\right)^2 & 0 & 0 \\ 0 & 1/\lambda_j^k & 0 \\ 0 & 0 & 1/\lambda_j^k \end{bmatrix} \tag{B. 1}$$

The total deformation gradient tensor $\mathbf{F}$ becomes

$$\mathbf{F} = \mathbf{F}_g^e \mathbf{F}_g^v \mathbf{F}_g^p \mathbf{F}_g^s \Rightarrow \lambda = \lambda_g^e \lambda_g^v \lambda_g^p \lambda_g^s \tag{B. 2}$$

where $\lambda = 1 + \varepsilon$. Substitution of $\mathbf{F}$, $\mathbf{F}_g^e$, $\mathbf{F}_g^v$, and $\mathbf{F}_g^p$ into Equation (25) and conversion to the Cauchy stress by multiplying $\mathbf{F}_g^v$ and $\left(\mathbf{F}_g^v\right)^T$ to the left and right side of every term, respectively, gives the following:

$$\mu_g \left(\lambda_g^v\right)^2 \frac{d\left(\lambda_g^v\right)^2}{dt} = \frac{1}{3}\left\{h\left(\lambda_g^e; C_{10,g}^e, C_{01,g}^e\right) - h\left(\lambda_g^v; C_{10,g}^v, C_{01,g}^v\right)\right\} + \frac{1}{2}\left(p_g^e - p_g^v\right) \tag{B. 3}$$

$$\mu_g \frac{1}{\lambda_g^v} \frac{d\left(1/\lambda_g^v\right)}{dt} = -\frac{1}{6}\left\{h\left(\lambda_g^e; C_{10,g}^e, C_{01,g}^e\right) - h\left(\lambda_g^v; C_{10,g}^v, C_{01,g}^v\right)\right\} + \frac{1}{2}\left(p_g^e - p_g^v\right) \tag{B. 4}$$

Subtracting Equation (B. 4) from Equation (B. 3) gives the final 1D equation for λ_g^v of glassy phase:

$$\mu_g \left\{ 2\left(\lambda_g^v\right)^3 + \frac{1}{\left(\lambda_g^v\right)^3} \right\} \frac{d\lambda_g^v}{dt} = \frac{1}{2}\left\{ h\left(\lambda_g^e; C_{10,g}^e, C_{01,g}^e\right) - h\left(\lambda_g^v; C_{10,g}^v, C_{01,g}^v\right) \right\} \tag{B. 5}$$

where $h\left(\lambda; C_{10}, C_{01}\right) = 2C_{10}\left(\lambda^2 - \lambda^{-1}\right) + 2C_{01}\left(\lambda - \lambda^{-2}\right)$ is the Cauchy stress determined by Mooney-Rivlin hyperelasticity.

Similarly, substitution of Equation (B. 1) into Equation (36) and converting it into the Cauchy stress using the relation $\boldsymbol{\sigma} = \frac{1}{J}\mathbf{F}\mathbf{S}\mathbf{F}^T$, the stress component of the glassy phase becomes

$$\sigma_{g,11} = \frac{4}{3}C_{10,g}^e \left\{ \left(\lambda_g^e\right)^2 - \frac{1}{\lambda_g^e} \right\} + \frac{4}{3}C_{01,g}^e \left\{ \lambda_g^e - \frac{1}{\left(\lambda_g^e\right)^2} \right\} + p_g^e \tag{B. 6}$$

$$\sigma_{g,22} = \sigma_{g,33} = -\frac{2}{3}C_{10,g}^e \left\{ \left(\lambda_g^e\right)^2 - \frac{1}{\lambda_g^e} \right\} - \frac{2}{3}C_{01,g}^e \left\{ \lambda_g^e - \frac{1}{\left(\lambda_g^e\right)^2} \right\} + p_g^e \tag{B. 7}$$

Considering the condition of the uniaxial extension, the Cauchy stress under this condition becomes

$$\begin{aligned} \sigma_g = \sigma_{g,11} - \sigma_{g,22} &= 2C_{10,g}^e \left\{ \left(\lambda_g^e\right)^2 - \frac{1}{\lambda_g^e} \right\} + 2C_{01,g}^e \left\{ \lambda_g^e - \frac{1}{\left(\lambda_g^e\right)^2} \right\} \\ &= h\left(\lambda_g^e; C_{10,g}^e, C_{01,g}^e\right) \end{aligned} \tag{B. 8}$$

Equations (B. 5) and (B. 8) form 1D constitutive equations for glassy phase. However, to determine the 1D constitutive model, λ_g^p and λ_g^s also must be known.

Substituting Equation (B. 1) into Equations (26) and (27) gives

$$\dot{\lambda}_g^p = \frac{1}{\mu_g^p}\langle f \rangle sign\left(\sigma_g\right) \tag{B. 9}$$

with $f = \sigma_g - \left\{\sigma^Y + E^p\left(\alpha^p\left(t\right)\right)^2\right\}$ and $\alpha^p\left(t\right) = \int_0^t \frac{\dot{\lambda}_g^p}{\lambda_g^p} d\tau$.

According to Equation (B. 1), the Lagrange strain $\mathbf{E}$, calculated from $\mathbf{C}$, is given by

$$\mathbf{E} = \frac{1}{2}\left(\mathbf{C} - \mathbf{I}\right) = \begin{bmatrix} \frac{\lambda^2 - 1}{2} & 0 & 0 \\ 0 & \frac{1/\lambda - 1}{2} & 0 \\ 0 & 0 & \frac{1/\lambda - 1}{2} \end{bmatrix} \tag{B. 10}$$

Because $\mathbf{E}$ is a diagonal matrix, substituting this into Equation (29) results in a diagonal matrix $\mathbf{E}_g^s$, where each diagonal value corresponds one of the principal stretches of the deformation gradient of shape memory strain, i.e., $\lambda_i^s = \sqrt{2E_{ii}^s + 1}$. By substituting these stretch values into Equation (32), $\mathbf{F}_g^s$ becomes

$$\mathbf{F}_g^s = \frac{1}{\left(J_g^s\right)^{1/3}} \begin{bmatrix} \lambda_{g,1}^s & 0 & 0 \\ 0 & \lambda_{g,2}^s & 0 \\ 0 & 0 & \lambda_{g,3}^s \end{bmatrix} \tag{B. 11}$$

The first component $\lambda_{g,1}^s$ is the strain in the extension direction, which corresponds to the value λ_g^s in Equation (B. 2).

B.3. 1D form of the model of the rubbery phase

The rubbery phase does not include a shape memory strain component in the model. Therefore, 1D constitutive equations for rubbery phase are written as similar form of Equations (B. 8) and (B. 5):

$$\sigma_r = h\left(\lambda_r^e; C_{10,r}^e, C_{01,r}^e\right) \tag{B. 12}$$

$$\mu_r \left\{ 2\left(\lambda_r^v\right)^3 + \frac{1}{\left(\lambda_r^v\right)^3} \right\} \frac{d\lambda_r^v}{dt} = \frac{1}{2}\left\{ h\left(\lambda_r^e; C_{10,r}^e, C_{01,r}^e\right) - h\left(\lambda_r^v; C_{10,r}^v, C_{01,r}^v\right) \right\} \tag{B. 13}$$

B.4. Fitting 1D equations in experimental results for obtaining parameters.

By volumetric combining Equations (B. 8) and (B. 12) with $\sigma = \xi_r \sigma_r + \xi_g \sigma_g$, the constitutive model for the shape memory effect in 1D form can be obtained.

By fitting the calculated uniaxial test at $T = T_l$ to experimentally measured values [Fig. B.1], the parameters in Equations (B. 8) and (B. 5) can be obtained, as listed in Table 1. Similarly, the parameters in Equations (B. 12) and (B. 13) can be obtained by fitting the test at $T = T_h$ [Fig. B.2]. The remaining parameters α and β can be calculated by fitting the models to the experimental results of the thermo-mechanical cyclic test [Fig. B.3]. Note that to impose the incompressibility of the material, the bulk moduli (κ) were assumed to be much larger than the stiffness of the hyperelastic springs so that the volume change is always within $100 \pm 2\%$.

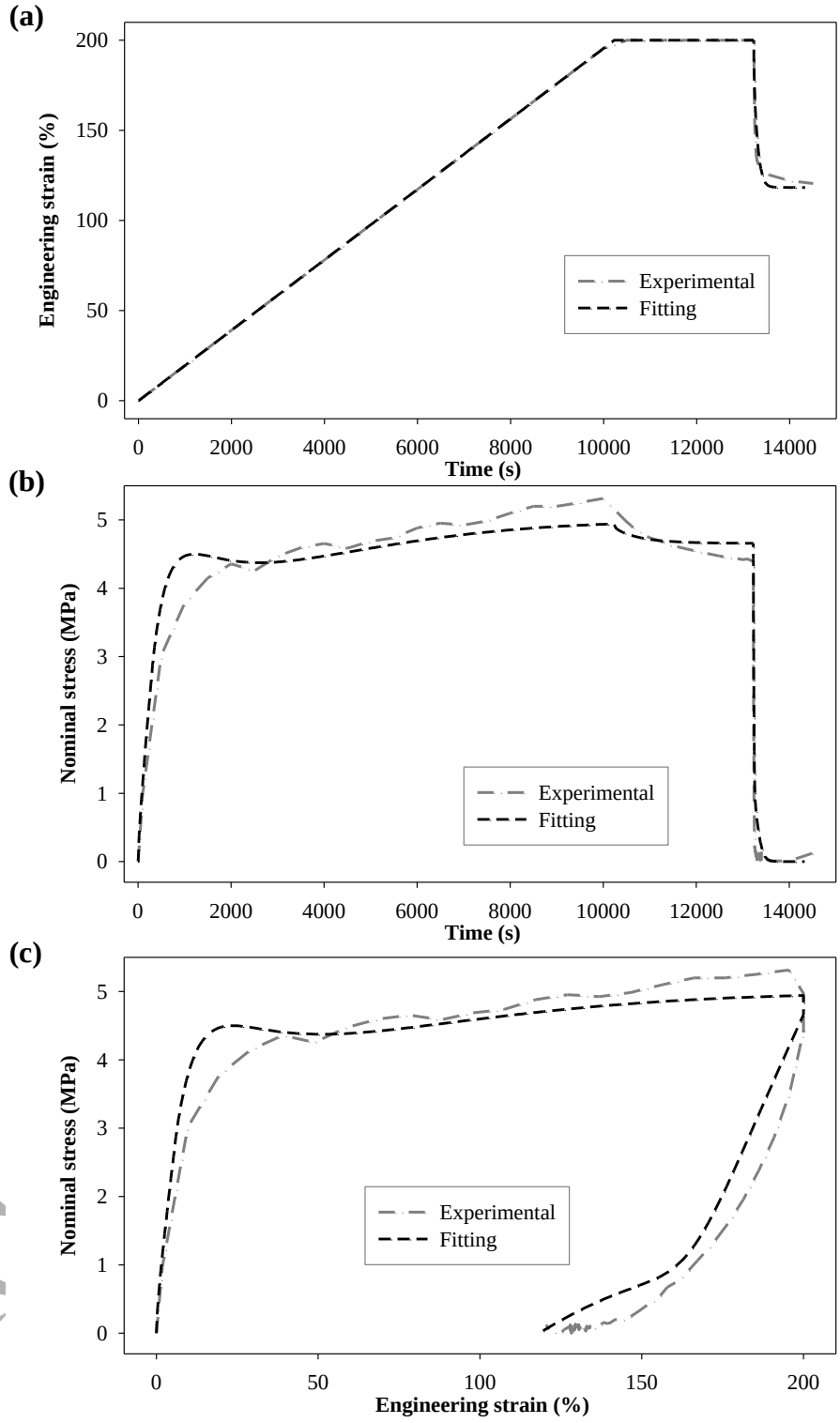

Fig. B.1. Experimental and fitting results of uniaxial extension and unloading test at $T = T_l$: (a) strain-time, (b) stress-time, and (c) stress-strain curves.

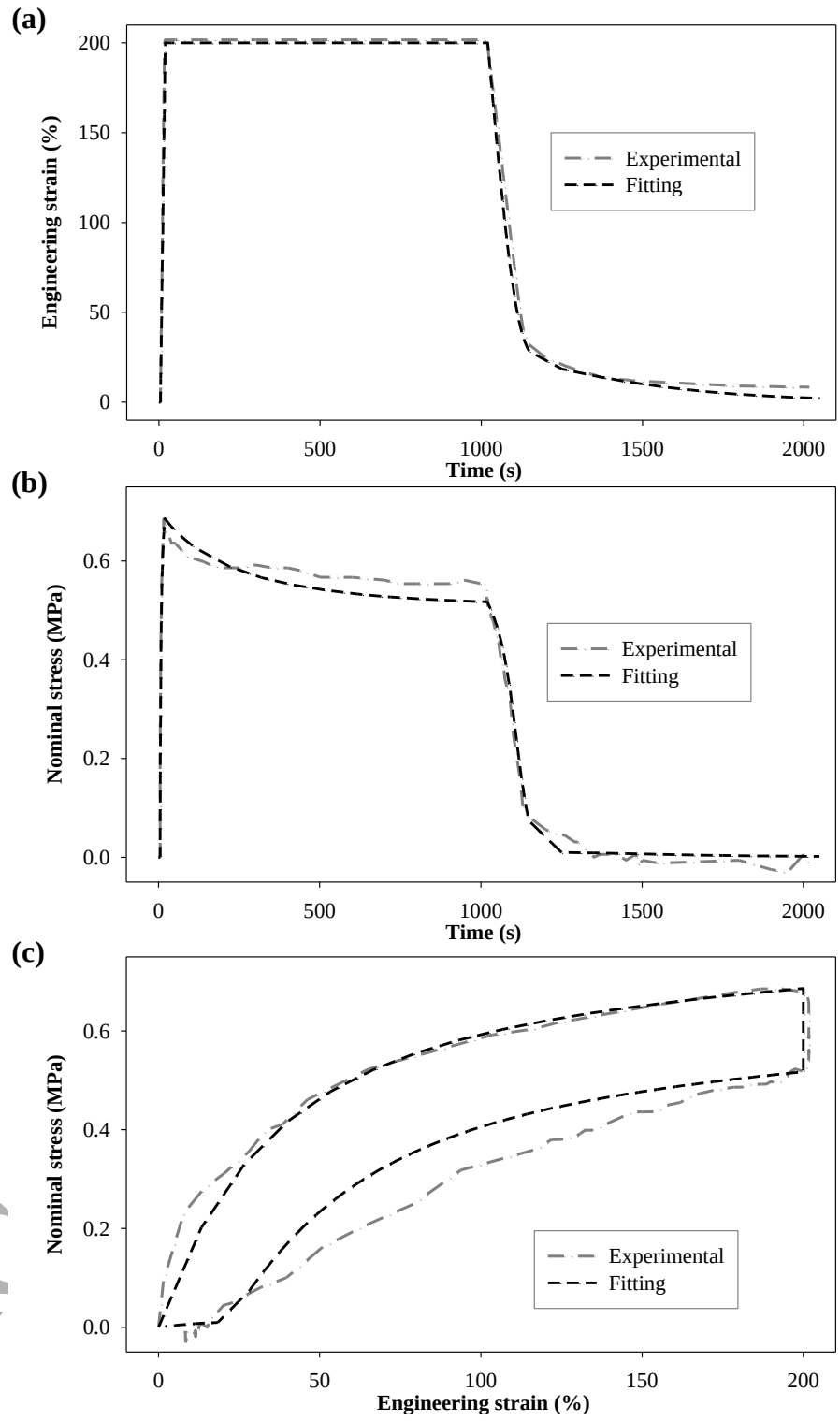

Fig. B.2. Experimental and fitting results of the uniaxial extension and unloading test at $T = T_h$: (a) strain-time, (b) stress-time, and (c) stress-strain curves.

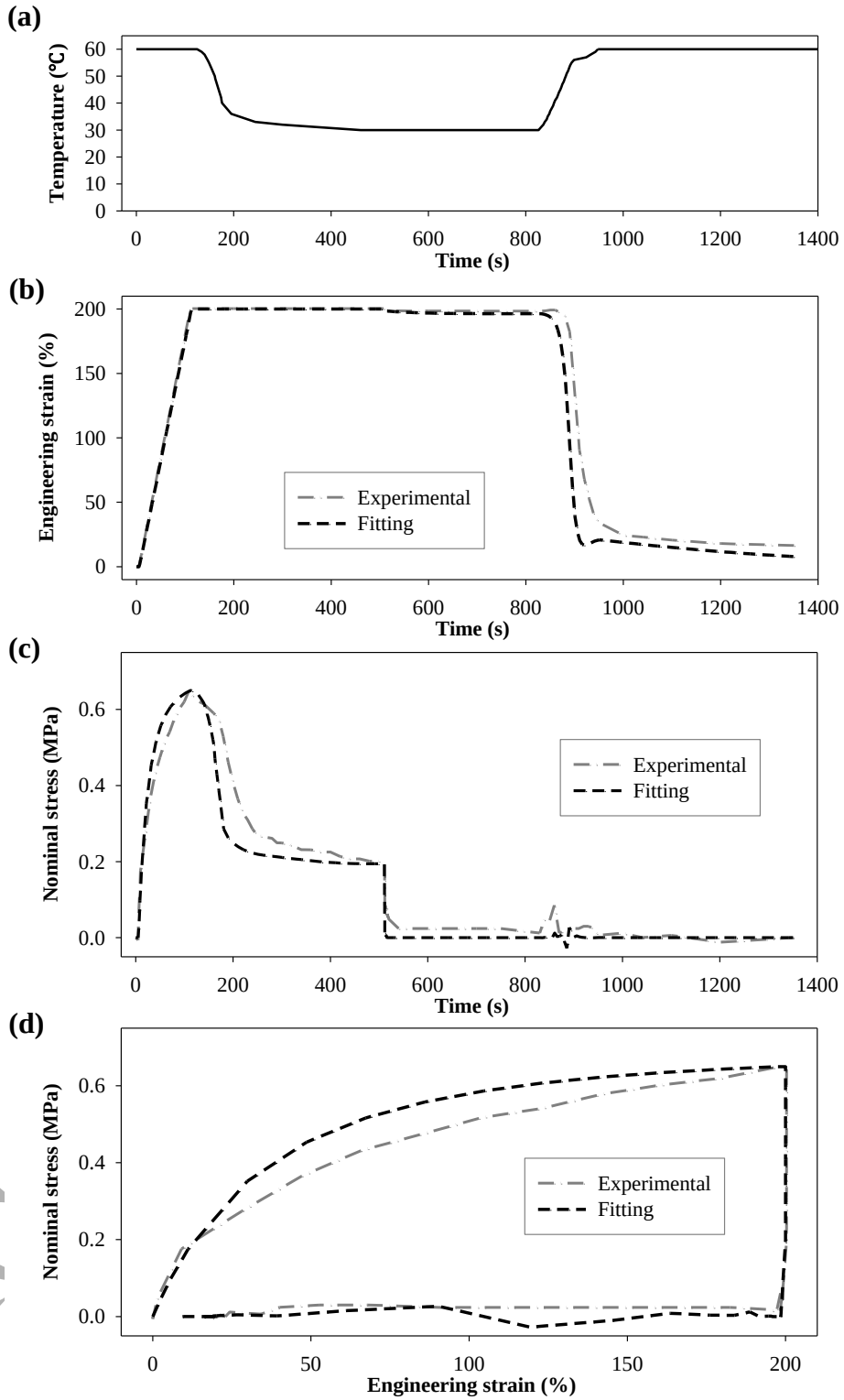

Fig. B.3. Experimental fitting results of the thermo-mechanical cyclic test: (a) input temperature, (b) strain-time, (c) stress-time, (d) stress-strain curves.

Appendix C. Thermal characterization

To measure the melting and crystallization temperatures of the PCO sample, differential scanning calorimetry (DSC, Mettler Toledo DSC 823E) was used. Heating was applied from 0 to 200 °C at a rate of 5 °C/min, followed by cooling from 200 °C to 0 at rate of -5 °C/min. Fig. C.1 below shows that the melting and crystallization temperatures of the PCO sample were 55.3 °C and 31.0 °C, respectively. The midpoint of these two was 43.15 °C, which was similar to the transition temperature of 44.3 °C obtained in Appendix A. We determined the temperature range (30 to 60 °C) for shape memory behavior by taking $T_h = T_{tr}$ +15 ºC and $T_l = T_{tr}$ -15 ºC.

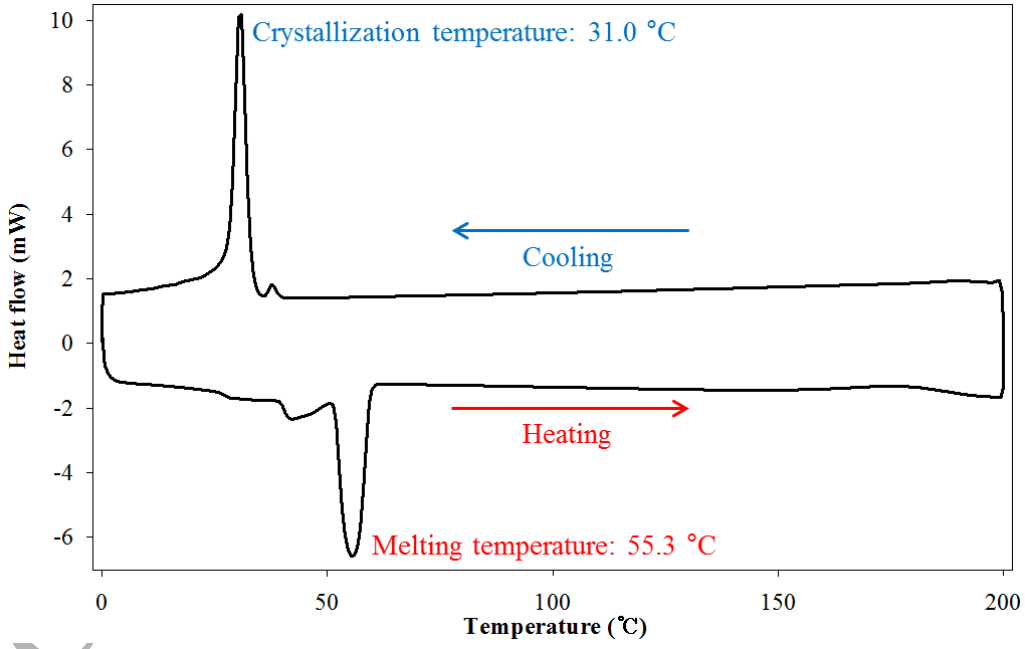

Fig. C.1. DSC thermogram of PCO sample.

References

Abrahamson, E.R., Lake, M.S., Munshi, N.A., Gall, K., 2003. Shape Memory Mechanics of an Elastic Memory Composite Resin. Journal of Intelligent Material Systems and Structures 14, 623-632.
Amestoy, P.R., Guermouche, A., L'Excellent, J.-Y., Pralet, S., 2006. Hybrid scheduling for the parallel solution of linear systems. Parallel Computing 32, 136-156.
Arruda, E.M., Boyce, M.C., 1993. A three-dimensional constitutive model for the large stretch behavior of rubber elastic materials. Journal of the Mechanics and Physics of Solids 41, 389-412.
Baghani, M., 2014. Analytical study on torsion of shape-memory-polymer prismatic bars with rectangular cross-sections. International Journal of Engineering Science 76, 1-11.
Baghani, M., Arghavani, J., Naghdabadi, R., 2014a. A finite deformation constitutive model for shape memory polymers based on Hencky strain. Mechanics of Materials 73, 1-10.
Baghani, M., Mohammadi, H., Naghdabadi, R., 2014b. An analytical solution for shape-memory-polymer Euler–Bernoulli beams under bending. International Journal of Mechanical Sciences 84, 84-90.
Baghani, M., Naghdabadi, R., Arghavani, J., 2012a. A large deformation framework for shape memory polymers: Constitutive modeling and finite element implementation. Journal of Intelligent Material Systems and Structures 24, 21-32.
Baghani, M., Naghdabadi, R., Arghavani, J., Sohrabpour, S., 2012b. A constitutive model for shape memory polymers with application to torsion of prismatic bars. Journal of Intelligent Material Systems and Structures 23, 107-116.
Baghani, M., Naghdabadi, R., Arghavani, J., Sohrabpour, S., 2012c. A thermodynamically-consistent 3D constitutive model for shape memory polymers. International Journal of Plasticity 35, 13-30.
Barot, G., Rao, I.J., 2006. Constitutive modeling of the mechanics associated with crystallizable shape memory polymers. Z. angew. Math. Phys. 57, 652-681.
Barot, G., Rao, I.J., Rajagopal, K.R., 2008. A thermodynamic framework for the modeling of crystallizable shape memory polymers. International Journal of Engineering Science 46, 325-351.
Bhattacharyya, A., Tobushi, H., 2000. Analysis of the isothermal mechanical response of a shape memory polymer rheological model. Polymer Engineering & Science 40, 2498-2510.
Boukamel, A., Gabrieli, C., Méo, S., 1997. Modélisation en grandes déformations viscoélastiques des élastomères. Actes du Troisième Colloque National en Calcul des Structures, 387-396.
Bower, A.F., 2009. Applied Mechanics of Solids. CRC Press.
Chen, J., Liu, L., Liu, Y., Leng, J., 2014. Thermoviscoelastic shape memory behavior for epoxy-shape memory polymer. Smart Materials and Structures 23, 055025.
Chen, Y.-C., Lagoudas, D.C., 2008a. A constitutive theory for shape memory polymers. Part I: Large deformations. Journal of the Mechanics and Physics of Solids 56, 1752-1765.
Chen, Y.-C., Lagoudas, D.C., 2008b. A constitutive theory for shape memory polymers. Part II: A linearized model for small deformations. Journal of the Mechanics and Physics of Solids 56, 1766-1778.
Chung, T., Romo-Uribe, A., Mather, P.T., 2007. Two-Way Reversible Shape Memory in a Semicrystalline Network. Macromolecules 41, 184-192.
Diani, J., Gilormini, P., Frédy, C., Rousseau, I., 2012. Predicting thermal shape memory of crosslinked polymer networks from linear viscoelasticity. International Journal of Solids and Structures 49, 793-799.
Diani, J., Liu, Y., Gall, K., 2006. Finite strain 3D thermoviscoelastic constitutive model for shape memory polymers. Polymer Engineering & Science 46, 486-492.
El Feninat, F., Laroche, G., Fiset, M., Mantovani, D., 2002. Shape Memory Materials for Biomedical Applications. Advanced Engineering Materials 4, 91-104.
Ge, Q., Dunn, C.K., Qi, H.J., Dunn, M.L., 2014. Active origami by 4D printing. Smart Materials and Structures 23, 094007.
Ge, Q., Qi, H.J., Dunn, M.L., 2013. Active materials by four-dimension printing. Applied Physics Letters 103, 131901.

Ghosh, P., Srinivasa, A.R., 2013. A two-network thermomechanical model and parametric study of the response of shape memory polymers. Mechanics of Materials 60, 1-17.
Ghosh, P., Srinivasa, A.R., 2014. Development of a finite strain two-network model for shape memory polymers using QR decomposition. International Journal of Engineering Science 81, 177-191.
Gilormini, P., Diani, J., 2012. On modeling shape memory polymers as thermoelastic two-phase composite materials. Comptes Rendus Mécanique 340, 338-348.
Gu, J., Sun, H., Fang, C., 2015. A multi-branch finite deformation constitutive model for a shape memory polymer based syntactic foam. Smart Materials and Structures 24, 025011.
Guo, X., Liu, L., Liu, Y., Zhou, B., Leng, J., 2014. Constitutive model for a stress- and thermal-induced phase transition in a shape memory polymer. Smart Materials and Structures 23, 105019.
Guo, X., Liu, L., Zhou, B., Liu, Y., Leng, J., 2015. Constitutive model for shape memory polymer based on the viscoelasticity and phase transition theories. Journal of Intelligent Material Systems and Structures.
Haupt, P., 2002. Continuum Mechanics and Theory of Materials. Springer Verlag, Berlin.
Helm, D., Haupt, P., 2003. Shape memory behaviour: modelling within continuum thermomechanics. International Journal of Solids and Structures 40, 827-849.
Heuchel, M., Sauter, T., Kratz, K., Lendlein, A., 2013. Thermally induced shape-memory effects in polymers: Quantification and related modeling approaches. J. Polym. Sci. B: Polym. Phys. 51, 621-637.
Hong, S.J., Yu, W.-R., Youk, J.H., 2008. Mechanical behavior of shape memory fibers spun from nanoclay-tethered polyurethanes. Macromol. Res. 16, 644-650.
Hong, S.J., Yu, W.-R., Youk, J.H., 2010. Two-way shape memory behavior of shape memory polyurethanes with a bias load. Smart Materials and Structures 19, 035022.
Hong, S.J., Yu, W.-R., Youk, J.H., Cho, Y.R., 2007. Polyurethane smart fiber with shape memory function: Experimental characterization and constitutive modelling. Fibers Polym 8, 377-385.
Kazakevičiūtė-Makovska, R., Heuchel, M., Kratz, K., Steeb, H., 2014. Universal relations in linear thermoelastic theories of thermally-responsive shape memory polymers. International Journal of Engineering Science 82, 140-158.
Kim, J.H., Kang, T.J., Yu, W.-R., 2010a. Simulation of mechanical behavior of temperature-responsive braided stents made of shape memory polyurethanes. Journal of Biomechanics 43, 632-643.
Kim, J.H., Kang, T.J., Yu, W.-R., 2010b. Thermo-mechanical constitutive modeling of shape memory polyurethanes using a phenomenological approach. International Journal of Plasticity 26, 204-218.
Laiarinandrasana, L., Piques, R., Robisson, A., 2003. Visco-hyperelastic model with internal state variable coupled with discontinuous damage concept under total Lagrangian formulation. International Journal of Plasticity 19, 977-1000.
Lan, X., Liu, L., Liu, Y., Leng, J., Du, S., 2014. Post microbuckling mechanics of fibre-reinforced shape-memory polymers undergoing flexure deformation. Mechanics of Materials 72, 46-60.
Lee, E.H., 1969. Elastic-Plastic Deformation at Finite Strains. Journal of Applied Mechanics 36, 1-6.
Lee, S.H., Kim, J.W., Kim, B.K., 2004. Shape memory polyurethanes having crosslinks in soft and hard segments. Smart Materials and Structures 13, 1345-1350.
Lejeunes, S., Boukamel, A., Méo, S., 2011. Finite element implementation of nearly-incompressible rheological models based on multiplicative decompositions. Computers & Structures 89, 411-421.
Leng, J., Lan, X., Liu, Y., Du, S., 2011. Shape-memory polymers and their composites: Stimulus methods and applications. Progress in Materials Science 56, 1077-1135.
Li, G., Shojaei, A., 2012. A viscoplastic theory of shape memory polymer fibres with application to self-healing materials. Proceedings of the Royal Society A: Mathematical, Physical and Engineering Science.
Lin, J.R., Chen, L.W., 1999. Shape-memorized crosslinked ester-type polyurethane and its mechanical viscoelastic model. Journal of Applied Polymer Science 73, 1305-1319.
Liu, C., Chun, S.B., Mather, P.T., Zheng, L., Haley, E.H., Coughlin, E.B., 2002. Chemically Cross-Linked Polycyclooctene: Synthesis, Characterization, and Shape Memory Behavior. Macromolecules 35, 9868-9874.
Liu, Y., Du, H., Liu, L., Leng, J., 2014. Shape memory polymers and their composites in aerospace

applications: a review. Smart Materials and Structures 23, 023001.
Liu, Y., Gall, K., Dunn, M.L., Greenberg, A.R., Diani, J., 2006. Thermomechanics of shape memory polymers: Uniaxial experiments and constitutive modeling. International Journal of Plasticity 22, 279-313.
Meo, S., Boukamel, A., Debordes, O., 2002. Analysis of a thermoviscoelastic model in large strain. Computers & Structures 80, 2085-2098.
Morshedian, J., Khonakdar, H.A., Rasouli, S., 2005. Modeling of Shape Memory Induction and Recovery in Heat-Shrinkable Polymers. Macromolecular Theory and Simulations 14, 428-434.
Nguyen, T.D., Qi, H.J., Castro, F., Long, K.N., 2008. A thermoviscoelastic model for amorphous shape memory polymers: Incorporating structural and stress relaxation. Journal of the Mechanics and Physics of Solids 56, 2792-2814.
Nguyen, T.D., Yakacki, C.M., Brahmbhatt, P.D., Chambers, M.L., 2010. Modeling the Relaxation Mechanisms of Amorphous Shape Memory Polymers. Advanced Materials 22, 3411-3423.
Pandini, S., Passera, S., Messori, M., Paderni, K., Toselli, M., Gianoncelli, A., Bontempi, E., Riccò, T., 2012. Two-way reversible shape memory behaviour of crosslinked poly(ε-caprolactone). Polymer 53, 1915-1924.
Perzyna, P., 1966. Fundamental Problems in Viscoplasticity. Advances in Applied Mechanics 9, 243-377.
Ping, P., Wang, W.S., Chen, X.S., Jing, X.B., 2007. The influence of hard-segments on two-phase structure and shape memory properties of PCL-based segmented polyurethanes. J. Polym. Sci. B: Polym. Phys. 45, 557-570.
Qi, H.J., Nguyen, T.D., Castro, F., Yakacki, C.M., Shandas, R., 2008. Finite deformation thermo-mechanical behavior of thermally induced shape memory polymers. Journal of the Mechanics and Physics of Solids 56, 1730-1751.
Qiao, T., Liu, L., Liu, Y., Leng, J., 2013. Post buckling analysis of the shape memory polymer composite laminate bonded with alloy film. Composites Part B: Engineering 53, 218-225.
Rao, I.J., Rajagopal, K.R., 2001. A study of strain-induced crystallization of polymers. International Journal of Solids and Structures 38, 1149-1167.
Reese, S., Böl, M., Christ, D., 2010. Finite element-based multi-phase modelling of shape memory polymer stents. Computer Methods in Applied Mechanics and Engineering 199, 1276-1286.
Richard, B., Lisa Mauck, W., 2008. Strain induced anisotropic properties of shape memory polymer. Smart Materials and Structures 17, 055021.
Schenk, O., Gärtner, K., 2004. Solving unsymmetric sparse systems of linear equations with PARDISO. Future Generation Computer Systems 20, 475-487.
Song, W., Wang, L., Wang, Z., 2011. Synthesis and thermomechanical research of shape memory epoxy systems. Materials Science and Engineering: A 529, 29-34.
Srivastava, V., Chester, S.A., Anand, L., 2010. Thermally actuated shape-memory polymers: Experiments, theory, and numerical simulations. Journal of the Mechanics and Physics of Solids 58, 1100-1124.
Tan, Q., Liu, L., Liu, Y., Leng, J., 2014. Thermal mechanical constitutive model of fiber reinforced shape memory polymer composite: Based on bridging model. Composites Part A: Applied Science and Manufacturing 64, 132-138.
Tobushi, H., Hara, H., Yamada, E., Hayashi, S., 1996. Thermomechanical properties in a thin film of shape memory polymer of polyurethane series. Smart Materials and Structures 5, 483-491.
Tobushi, H., Okumura, K., Hayashi, S., Ito, N., 2001. Thermomechanical constitutive model of shape memory polymer. Mechanics of Materials 33, 545-554.
Wang, Z., Li, D.F., Xiong, Z., Chang, R.N., 2009. Modeling thermomechanical behaviors of shape memory polymer. Journal of Applied Polymer Science 113, 651-656.
Wang, Z., Li, Z., 2011. Theoretical analysis of the deformation of SMP sandwich beam in flexure. Archive of Applied Mechanics 81, 1667-1678.
Wang, Z., Li, Z., Wang, L., Xiong, Z., Zhengdao, W., Li, Z., Wang, L., Xiong, Z., 2010. Viscoelastic characteristics of shape memory polymers. Journal of Applied Polymer Science 118, 1406-1413.
Westbrook, K.K., Kao, P.H., Castro, F., Ding, Y., Qi, H.J., 2011. A 3D finite deformation constitutive model for amorphous shape memory polymers: A multi-branch modeling approach for nonequilibrium

relaxation processes. Mechanics of Materials 43, 853-869.
Westbrook, K.K., Parakh, V., Chung, T., Mather, P.T., Wan, L.C., Dunn, M.L., Qi, H.J., 2010. Constitutive Modeling of Shape Memory Effects in Semicrystalline Polymers With Stretch Induced Crystallization. Journal of Engineering Materials and Technology 132, 041010-041019.
Xiao, R., Choi, J., Lakhera, N., Yakacki, C.M., Frick, C.P., Nguyen, T.D., 2013. Modeling the glass transition of amorphous networks for shape-memory behavior. Journal of the Mechanics and Physics of Solids 61, 1612-1635.
Xiao, R., Nguyen, T.D., 2013. Modeling the solvent-induced shape-memory behavior of glassy polymers. Soft Matter 9, 9455-9464.
Xiao, X., Kong, D., Qiu, X., Zhang, W., Zhang, F., Liu, L., Liu, Y., Zhang, S., Hu, Y., Leng, J., 2015. Shape-Memory Polymers with Adjustable High Glass Transition Temperatures. Macromolecules 48, 3582–3589.
Xu, W., Li, G., 2010. Constitutive modeling of shape memory polymer based self-healing syntactic foam. International Journal of Solids and Structures 47, 1306-1316.
Yang, Q., Stainier, L., Ortiz, M., 2006. A variational formulation of the coupled thermo-mechanical boundary-value problem for general dissipative solids. Journal of the Mechanics and Physics of Solids 54, 401-424.
Yu, K., Ritchie, A., Mao, Y., Dunn, M.L., Qi, H.J., 2015. Controlled Sequential Shape Changing Components by 3D Printing of Shape Memory Polymer Multimaterials. Procedia IUTAM 12, 193-203.
Zhang, F., Zhang, Z., Liu, Y., Cheng, W., Huang, Y., Leng, J., 2015. Thermosetting epoxy reinforced shape memory composite microfiber membranes: Fabrication, structure and properties. Composites Part A: Applied Science and Manufacturing 76, 54-61.